Supplementary Information

Solvation chemistry tailored via dielectric constant engineering for stable low-temperature aqueous zinc batteries

Xiaoqing Zhu[1,#], Zilong Wang[2,#], Tao Zhang[1], Jia Zhang[1], Aimin Ge[1], Yunteng Cao[3], Rui Gao[4], Zhipeng Yu[5], Yuhao Wang[2], Shengjun Xu[6,7], Ho Mei Law[6,7], Fei Wang[8], Francesco Ciucci[2,6,7*], Guiyin Xu[1,9*], Meifang Zhu[1]

[1]State Key Laboratory of Advanced Fiber Materials, College of Materials Science and Engineering, Donghua University, Shanghai 201620, China

[2]Department of Mechanical and Aerospace Engineering, The Hong Kong University of Science and Technology, Clear Water Bay, Kowloon, Hong Kong S.A.R., China

[3]Department of Molecular, Cellular and Developmental Biology, Yale University, New Haven, CT 06511, USA

[4]Department of Nuclear Science and Technology, Xi'an Jiaotong University, Xi'an 710049, China

[5]International Iberian Nanotechnology Laboratory (INL), Avenida Mestre Jose Veiga, Braga 4715-330, Portugal

[6]University of Bayreuth, Chair of Electrode Design for Electrochemical Energy, Bayreuth 95448, Germany

[7]Bavarian Center for Battery Technology (BayBatt), University of Bayreuth, Universitätsstr. 30, 95447 Bayreuth, Germany

[8]Department of Materials Science, Fudan University, Shanghai 200433, China

[9]Henan Academy of Sciences, Zhengzhou 450001, China

* Corresponding author. E-mail: francesco.ciucci@uni-bayreuth.de (Francesco Ciucci); xuguiyin@dhu.edu.cn (Guiyin Xu).

# These authors contributed equally.

Table of Contents

Supplementary Discussion

Discussion S1. Derivation of cell potential

Here the cell potential will be derived from the chemical potentials of the system. The two half reactions of our setup are as below:

$$Zn_{ref} \leftrightarrow Zn^{2+}_{EL_{ref}} + 2e^-_{ref} \quad (1)$$

$$Zn^{2+}_{EL_{test}} + 2e^-_{test} \leftrightarrow Zn_{test} \quad (2)$$

Since the cell is at open circuit, the reaction is at equilibrium (3). Equilibrium condition is as follows:

$$\overline{\mu}^{EL_{ref}}_{Zn^{2+}} + \overline{\mu}^{Zn_{ref}}_{e^-} + \overline{\mu}^{Zn_{test}}_{Zn} = \overline{\mu}^{EL_{test}}_{Zn^{2+}} + \overline{\mu}^{Zn_{test}}_{e^-} + \overline{\mu}^{Zn_{ref}}_{Zn} \quad (3)$$

Electrochemical potential is made up of two terms: the electrostatic potential term and the chemical potential term. The electrostatic portion of the metallic zinc is zero for both sides, as it is electrically neutral. The chemical potential of metallic zinc is equal on both sides. Therefore, the metallic zinc terms disappear entirely.

$$\mu^{EL_{ref}}_{Zn^{2+}} + F\varphi^{EL_{ref}} + \mu^{Zn_{ref}}_{e^-} - F\varphi^{Zn_{ref}} = \mu^{EL_{test}}_{Zn^{2+}} + F\varphi^{EL_{test}} + \mu^{Zn_{test}}_{e^-} - F\varphi^{Zn_{test}} \quad (4)$$

In equation 4, $\varphi^{EL_{ref}}$ and $\varphi^{EL_{test}}$ are equal. This is true because we have minimized the liquid junction potential using a salt bridge[1].

Also, $\mu^{Zn_{ref}}_{e^-}$ and $\mu^{Zn_{test}}_{e^-}$ are equal, as the chemical environments are equivalent in the two electrodes. The resulting equation is as follows:

$$\mu^{EL_{ref}}_{Zn^{2+}} - F\varphi^{Zn_{ref}} = \mu^{EL_{test}}_{Zn^{2+}} - F\varphi^{Zn_{test}} \quad (5)$$

Rearranging equation 5, we see that voltage of the cell, which is the difference in electrostatic potentials between the two electrodes, is dependent on the chemical potential difference in the two electrolyte phases.

$$E_{cell} = \varphi^{Zn_{ref}} - \varphi^{Zn_{test}} = \frac{\mu^{EL_{ref}}_{Zn^{2+}} - \mu^{EL_{test}}_{Zn^{2+}}}{F} \quad (6)$$

The impact of SEI on battery potential is not considered here[2,3]. There EL_{ref} is the reference electrolyte and EL_{test} is the test electrolyte.

Discussion S2. Salt-induced dielectric response regulation in incompatible solvent systems.

To rationalize the structure–activity relationship of the electrolyte, we introduce classical models for the principal intermolecular interactions (ion–ion, ion–dipole, and dipole–dipole). Their orientation-averaged potential energies are given by Eqs. (7)–(9) (SI units suppressed for clarity)[4,5].

$$U_{ion\text{-}ion}=-\frac{1}{4\pi\varepsilon}\frac{z_1 z_2 e^2}{r} \tag{7}$$

$$U_{ion\text{-}dipole}=-\frac{1}{4\pi\varepsilon}\frac{ze\mu\cos\theta}{r^2} \tag{8}$$

$$U_{dipole\text{-}dipole}=-\frac{1}{(4\pi\varepsilon)^2}\frac{2\mu_1^2\mu_2^2}{3k_B T r^6} \tag{9}$$

The dielectric constant epsilon quantifies the response to an applied field and arises microscopically from dipole orientation. In a simple mean-field picture, it scales with the effective molecular dipole moment and the number density of dipoles:

$$\varepsilon \propto \frac{\mu_1^2\mu_2^2}{k_B T} \tag{10}$$

Here, U denotes the interaction energy, ε is the dielectric constant, ze is the charge of the ion, μ is the dipole moment of the dipole, r is the distance between ions or the centers of dipoles, θ is the dipole angle relative to the line joining the ion and the center of the dipole, k_B is the Boltzmann constant, and T is the absolute temperature.

Electrolytes modify dielectric behavior through coordination and network effects. For example, Zn^{2+} forms $[Zn(H_2O)_6]^{2+}$ complexes, binding water and reducing the number density of free water dipoles, thereby lowering their dielectric contribution. At 25 °C, pure water has ε = 78.46[6], whereas a $Zn(ClO_4)_2$ aqueous solution exhibits epsilon ~ 45. In mixed EA/H_2O electrolytes, EA engages in dipole–dipole interactions with water, and the chaotropic anion ClO_4^- disrupts the water hydrogen-bond network. Both effects increase orientational disorder, reduce the effective vector sum of water dipoles, and diminish the bulk dielectric response. The resulting local dielectric shielding, integrated over the liquid, decreases the overall ε.

Supplementary Figures

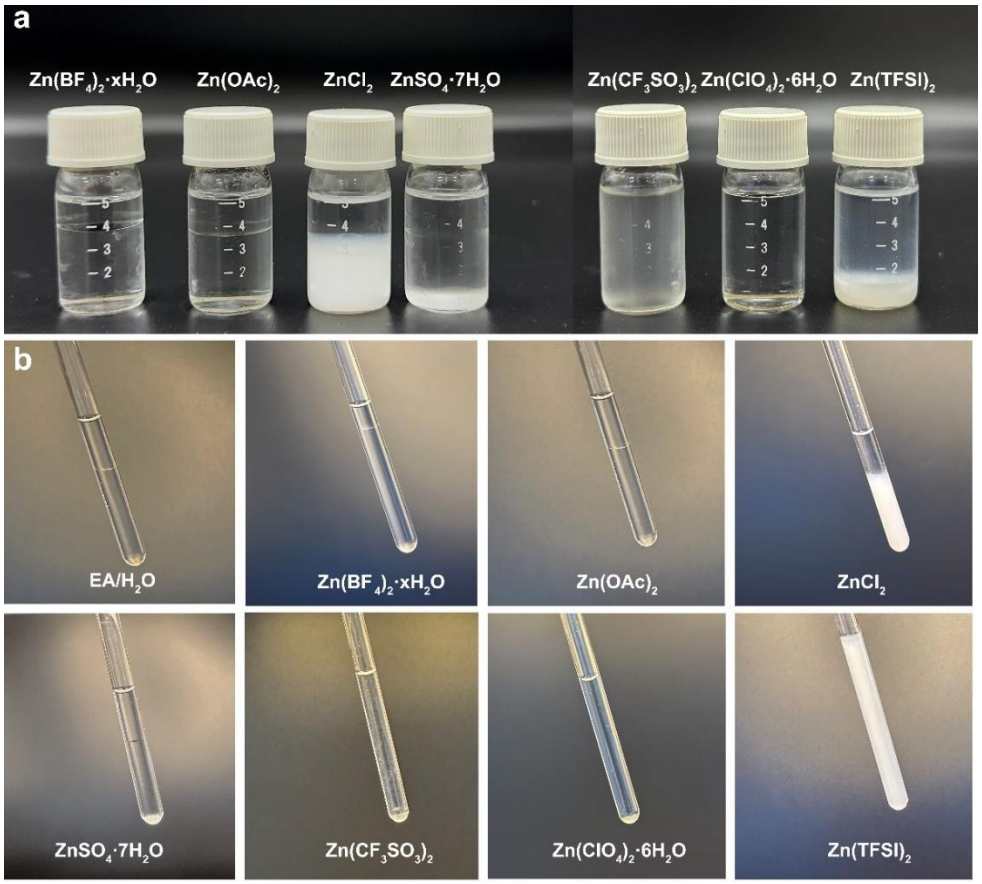

Supplementary Fig. 1 Solubility of various zinc salts in mixtures of EA and water (nEA:nH_2O = 1:16). (a) The 2 M electrolytes were prepared using various zinc salts with the solvents of EA and H_2O (nEA:nH_2O = 1:16). (b) The electrolytes were transferred into glass tubes to allow observation of its phase-separation behavior. It was observed that none of the Zn salts could form a homogeneous solution except $Zn(ClO_4)_2·6H_2O$. The solutions containing $Zn(BF_4)_2·xH_2O$, $ZnOAc_2$ and $ZnSO_4·7H_2O$ remained phase-separated, while the other solutions with undissolved zinc salts ($ZnCl_2$, $Zn(CF_3SO_3)_2$ and $Zn(TFSI)_2$). Additionally, $Zn(CF_3SO_3)_2$ enables miscibility of EA and water at a molar ratio of 1:16. Conductivity measurements indicate that $Zn(CF_3SO_3)_2$ in an EA:H_2O mixture (1:16 molar ratio) achieves a conductivity of 41.32 mS cm^{-1} at 25 °C and 10.56 mS cm^{-1} at −50 °C. In contrast, under the same conditions, $Zn(ClO_4)_2$ in EA:H_2O (1:16 molar ratio) exhibits higher conductivities of 64.47 mS cm^{-1} at 25 °C and 24.92 mS cm^{-1} at −50 °C. Thus, the $Zn(ClO_4)_2$-based electrolyte demonstrates superior conductivity at low temperatures, making it a promising candidate for cryogenic applications.

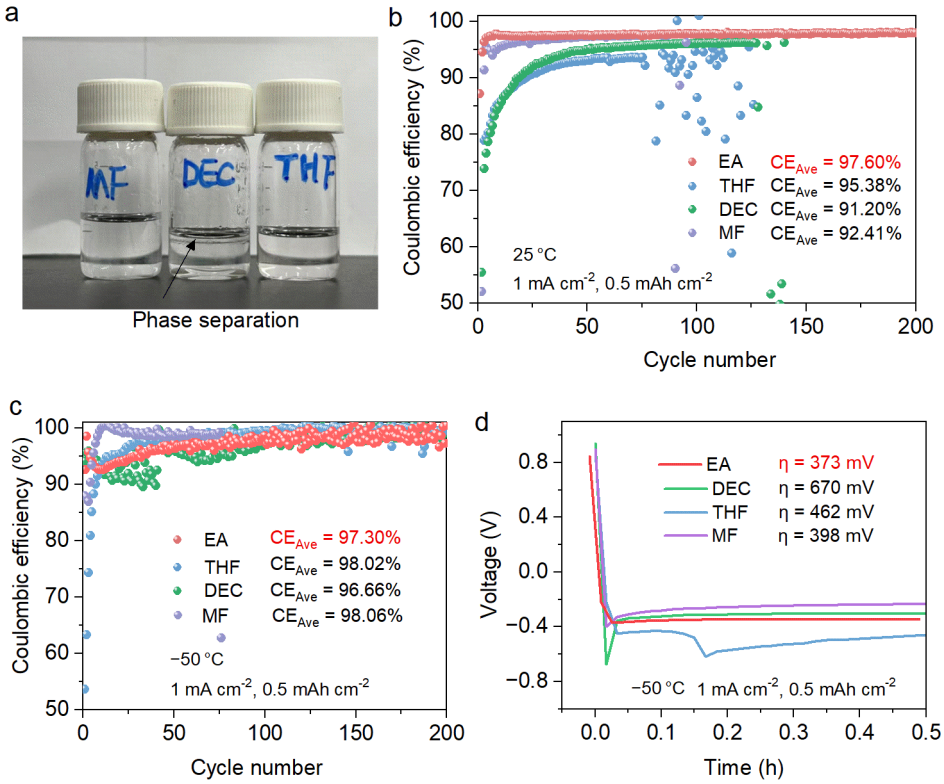

Supplementary Fig. 2 a, Digital photograph of an electrolyte containing low dielectric constant solvents such as THF, DEC, and MF. b, c The CEs of Zn||Cu batteries at a current density of 1 mA cm^{-2} and 0.5 mAh cm^{-2} at 25 °C (b) and −50 °C (c). d, The first discharge curve of Zn||Cu batteries at a current density of 1 mA cm^{-2} and an areal capacity of 0.5 mAh cm^{-2}.

Supplementary Note 1

To systematically evaluate the impact of low dielectric constant co-solvents on the low-temperature performance of batteries, we selected a series of solvents with similar dielectric constants, specifically diethyl carbonate (DEC) (ε = 2.8), tetrahydrofuran (THF) (ε = 7.4), and methyl formate (MF) (ε = 8.5). Our findings reveal that the electrolyte with DEC led to macroscopic phase separation (Supplementary Fig. 2a). Notably, THF and MF did not exhibit any layering. Zn||Cu batteries were assembled to investigate zinc ion plating and stripping at both room and low temperatures. The electrolyte containing DEC resulted in an average Coulombic efficiency of 91.2% at room temperature and 96.66% at low temperature (−50 °C), which is markedly lower than that of other electrolytes. Furthermore, the nucleation overpotential at low temperature (η = 670 mV) was significantly higher than that observed with different electrolytes (Supplementary Fig. 2b, c). As a result, EA exhibits particularly

outstanding low-temperature electrochemical performance. This provides an important design concept and research direction for the subsequent development of high-performance low-temperature resistant electrolyte systems.

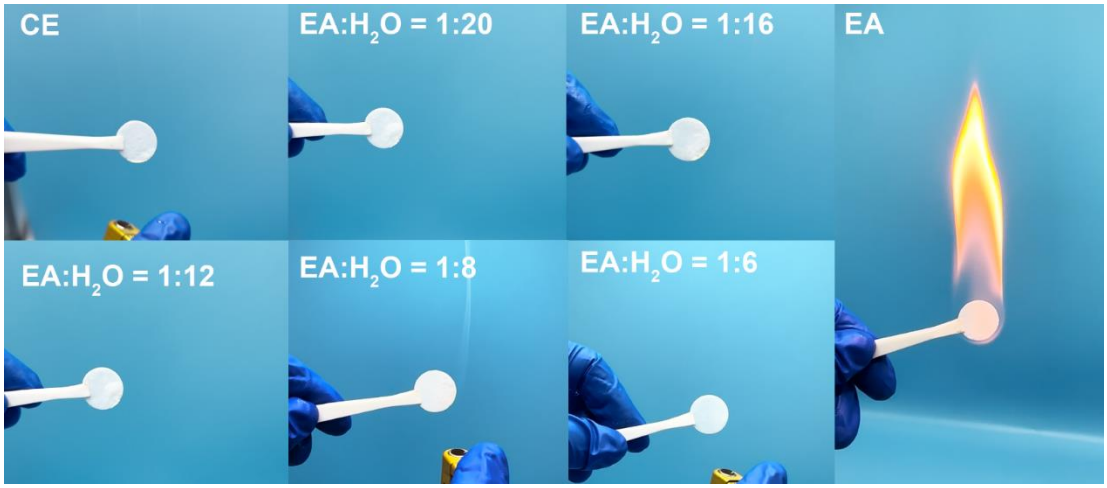

Supplementary Fig. 3 Digital images of flammability tests of the $Zn(ClO_4)_2$ H_2O/EA electrolytes with different molar ratios of EA/H_2O.

Supplementary Note 2

Initial safety assessments involved exposing glass fibers containing either electrolytes or pure EA solution to flame for 5 seconds. While the pure EA solution ignited readily, the hybrid electrolytes demonstrated robust flame retardance, establishing their safety for energy storage applications.

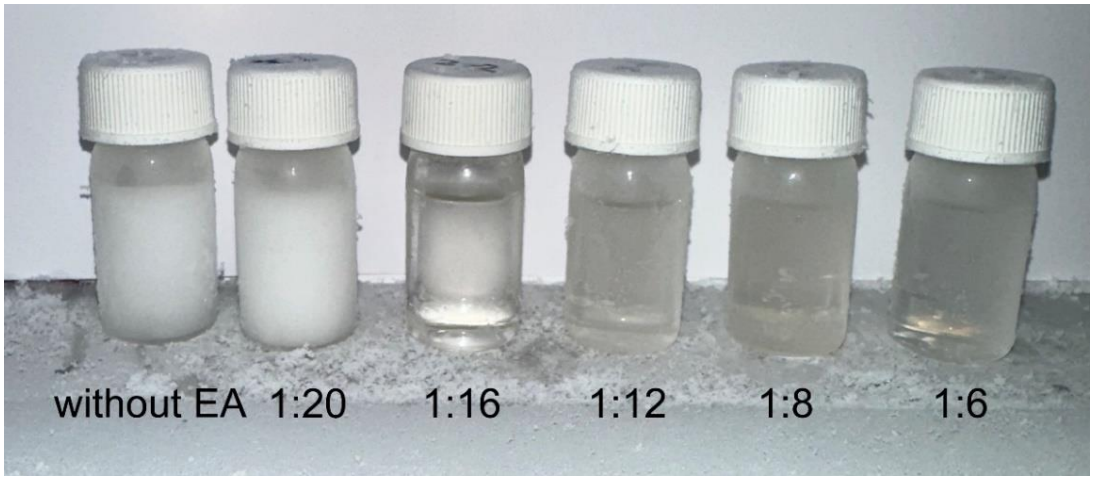

Supplementary Fig. 4 The digital images of freezing resistance test of the 2 M $Zn(ClO_4)_2$ H_2O/EA electrolytes with different molar ratios of EA/H_2O at −80 °C for 3 hours.

Supplementary Note 3

Low-temperature stability tests demonstrated that formulations with EA:H_2O ratios of 1:16 or higher remained in a liquid state without separation or precipitation when held at −80 °C for 3 hours. In contrast, pure water-based $Zn(ClO_4)_2$ electrolyte and the 1:20 EA:H_2O hybrid crystallized under these conditions.

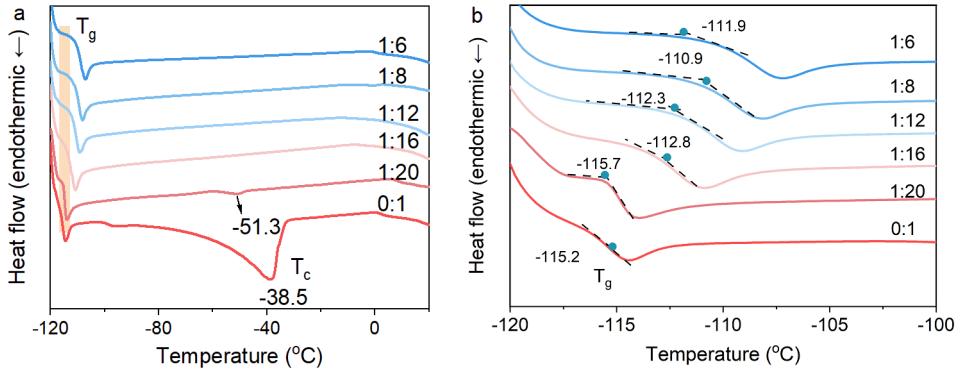

Supplementary Fig. 5 Low-temperature stability evaluation of the electrolytes. (a) DSC data of the $Zn(ClO_4)_2$ H_2O/EA mixtures with different EA/H_2O molar ratios (0:1, 1:20, 1:16, 1:12, 1:8 and 1:6), the measurements were conducted over a temperature range of 20°C-(-120°C), (b) All electrolytes exhibit glass transition temperatures below −110 °C.

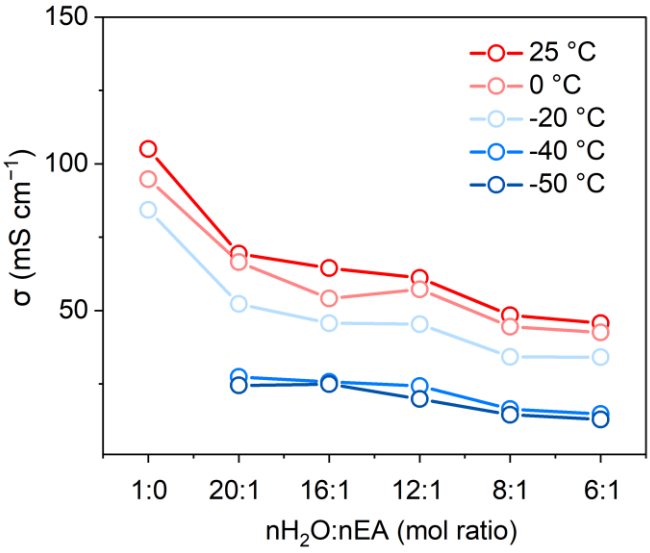

Supplementary Fig. 6 Temperature-dependent ionic conductivity of 2 M $Zn(ClO_4)_2$ in H_2O/EA as a function of EA:H_2O molar ratio (0:1 to 1:6), measured with a conductivity meter.

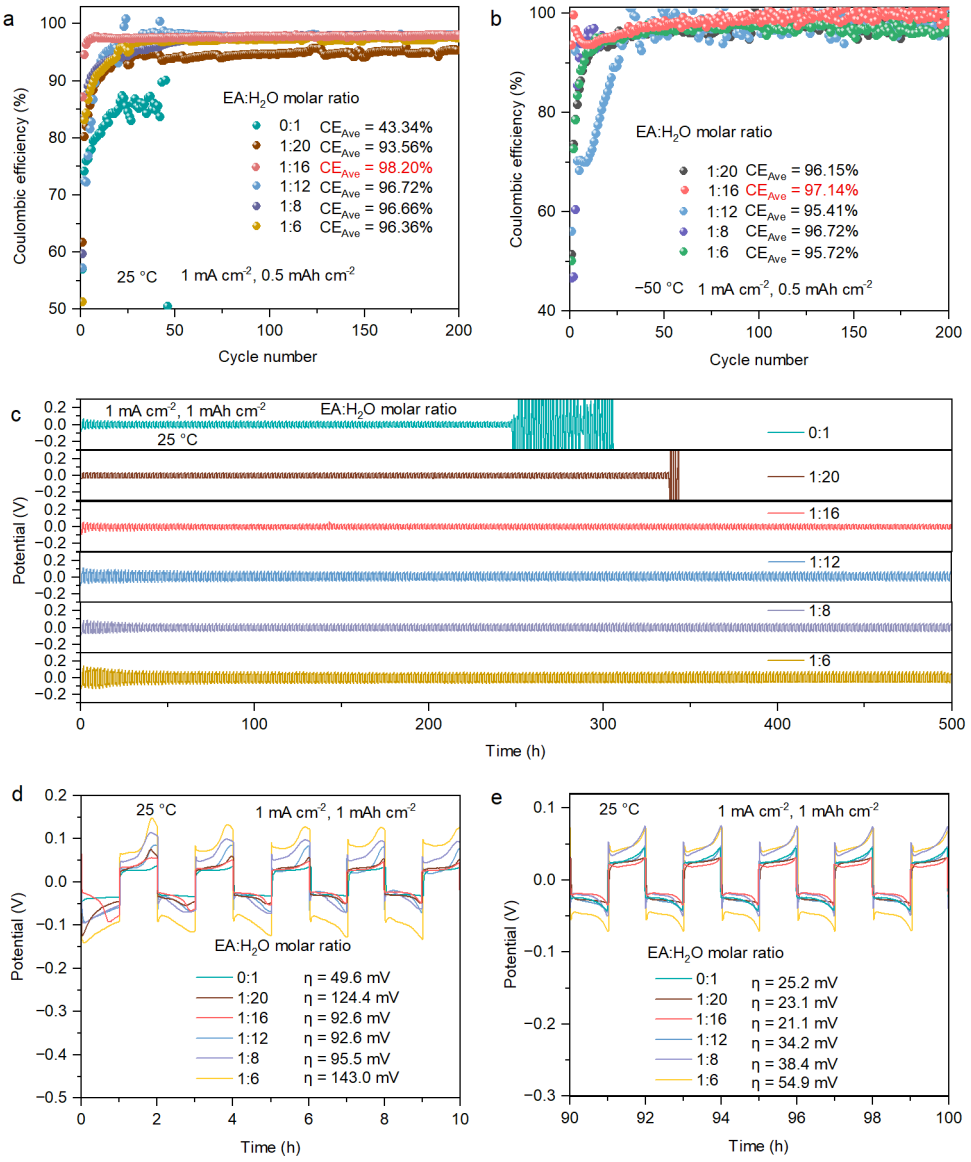

Supplementary Fig. 7 (a,b) Coulombic efficiency of Zn||Cu cells (1 mA cm^{-2}, 0.5 mAh cm^{-2}) at 25 °C (a) and -50 °C (b). (c-e) Zn plating/stripping of Zn||Zn cells at 1 mA cm^{-2} and 1 mAh cm^{-2}: (c) long-term performance, (d) time-resolved voltage profile at 0-10 h, and (e) at 90-100 h.

Supplementary Note 4

Zn||Cu asymmetric cells were assembled to assess Zn plating/stripping reversibility across EA:H_2O ratios from 0:1 to 1:6. As shown in Supplementary Fig. 7a,b, the MDCE (EA:H_2O = 1:16) delivered average Coulombic efficiencies of 98.2% at 25 °C and 97.14% at -50 °C, outperforming the other formulations. In contrast, the HDCE (0:1)

exhibited an operational life of only ~100 cycles with an average Coulombic efficiency of 43.34% and failed to operate at -50 °C.

Symmetric Zn||Zn cells were then used to probe plating/stripping stability (Supplementary Fig. 6c-e). Most EA-containing electrolytes showed markedly enhanced stability relative to 0:1 and 1:20 ratios. Notably, in the MDCE cell the overpotential decreased from 92.6 mV (0-10 h) to 21.1 mV (90-100 h), consistent with the formation of a stable, ion-conductive SEI during initial cycles. These results identify EA:H_2O = 1:16 as the optimal composition for MDCE.

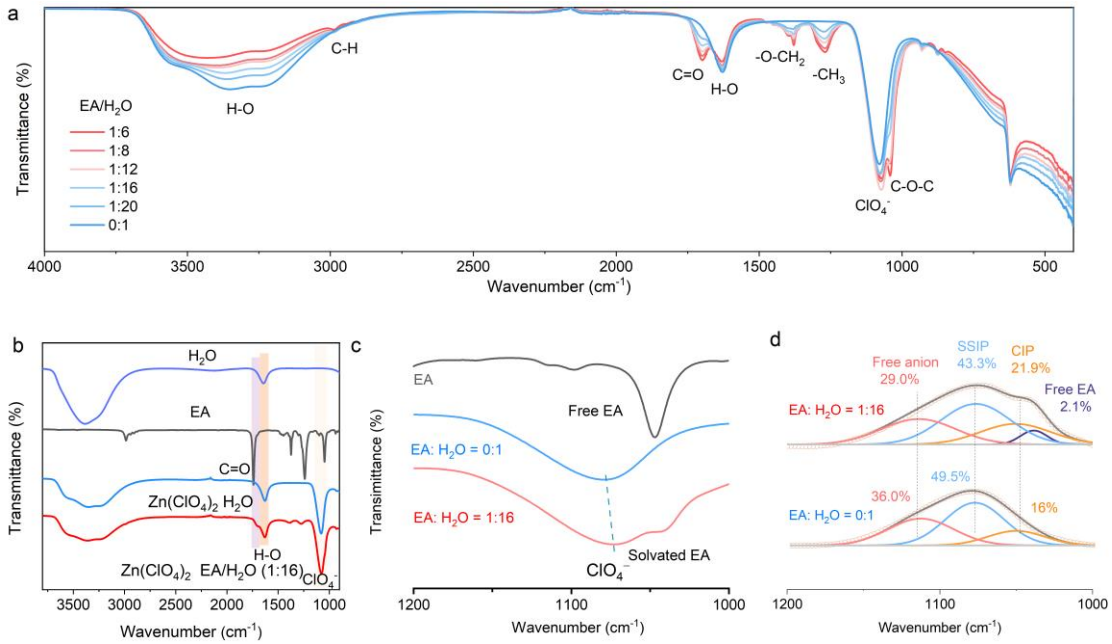

Supplementary Fig. 8 a, FTIR spectra of 2 M $Zn(ClO_4)_2$ H_2O/EA electrolytes with different EA/H_2O ratios from 0:1 to 1:6 at 4,000-400 cm^{-1}. b, c FTIR spectra of H_2O, EA, 2 M $Zn(ClO_4)_2$ H_2O and 2 M $Zn(ClO_4)_2$ EA/H_2O (EA:H_2O = 1:16) electrolytes at 3,800-800 cm^{-1} (b) and 1,200-1,000 cm^{-1} (c). d, Deconvolution result of FTIR spectra for 2 M $Zn(ClO_4)_2$ H_2O and 2 M $Zn(ClO_4)_2$ EA/H_2O (EA:H_2O = 1:16) electrolytes at and 1,200-1,000 cm^{-1}.

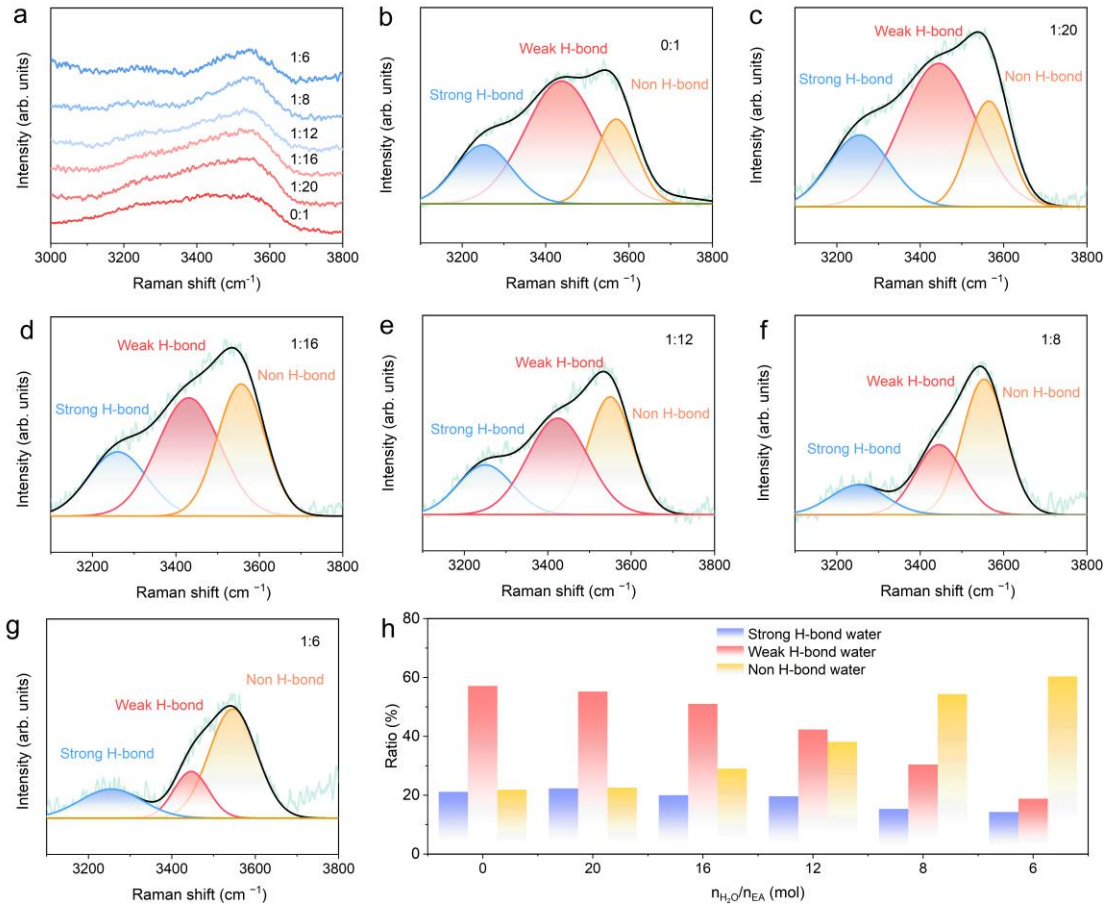

Supplementary Fig. 9 a, Raman spectra of d 2 M $Zn(ClO_4)_2$ H_2O/EA electrolytes at 3,800-3,000 cm^{-1}. b-g, The fitted O-H stretching vibration representing water molecules with strong, weak and non H-bonds of 2 M $Zn(ClO_4)_2$ H_2O/EA electrolytes with different EA/H_2O ratios from 0:1 to 1:6. h, The proportion of strong H-bond water, weak H-bond water, and non H-bond water.

Supplementary Note 5

Raman spectroscopy with hydrogen-bonded peaks in the 3,100 cm^{-1} to 3,700 cm^{-1} range (Supplementary Fig. 8a). As shown in Supplementary Fig. 8b-h, the area of peaks representing non-hydrogen-bonded water increases progressively to 60.3% with the rise in EA concentration, indicating the disruption of the hydrogen-bonding network of water.

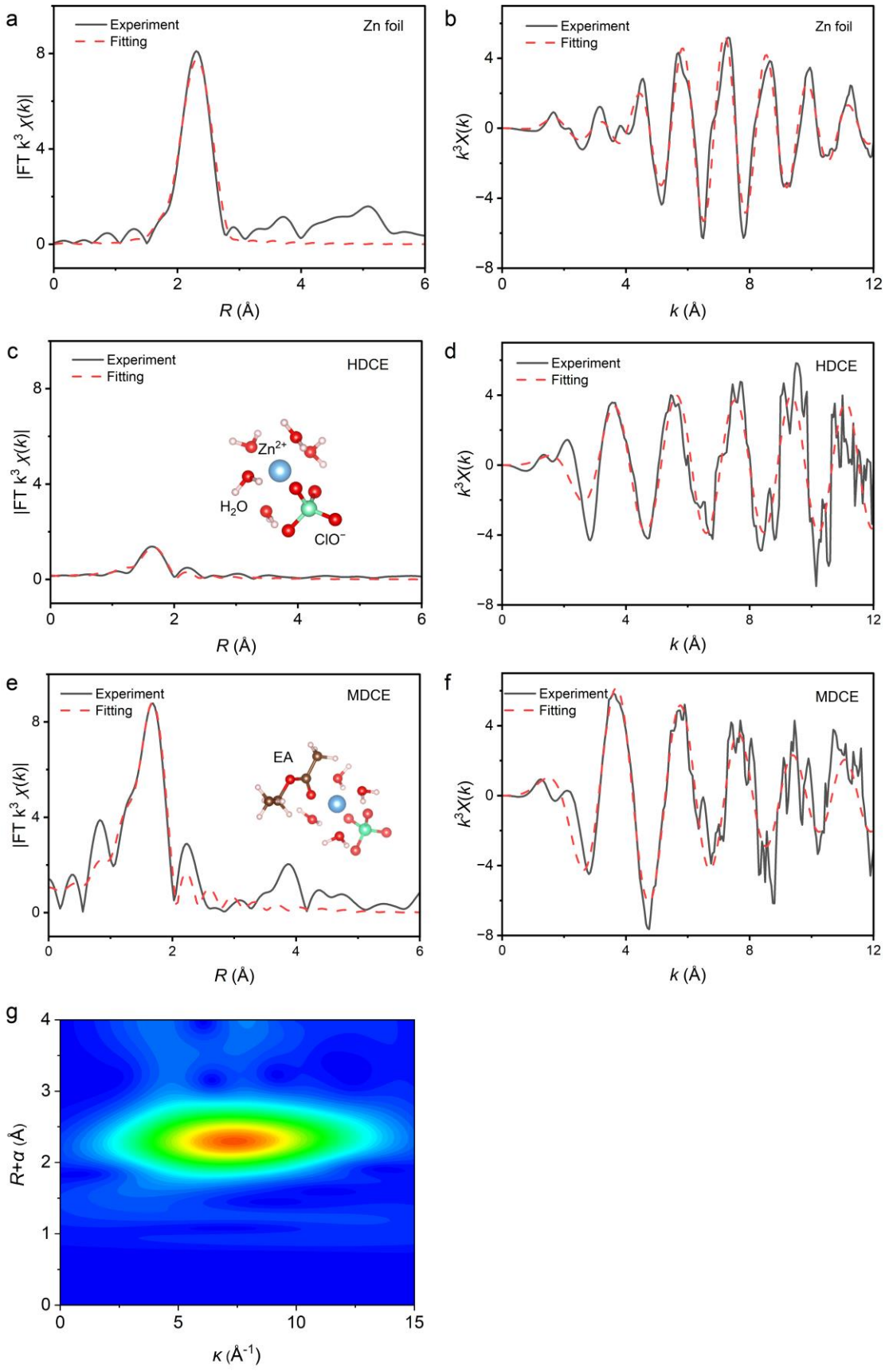

Supplementary Fig. 10 a, b Fitting of EXAFS spectra in R space (a) and k space (b) for Zn foil. c, d, e, f Fitting of EXAFS spectra in R space and k space for HDCE based

on DFT optimized molecular geometries of $[Zn(ClO_4)(H_2O)_5]^+$ (c, d) and MDCE based on DFT optimized molecular geometries of $[Zn(ClO_4)EA(H_2O)_4]^+$ (e, f). (g) Wavelet transforms for the Zn foil.

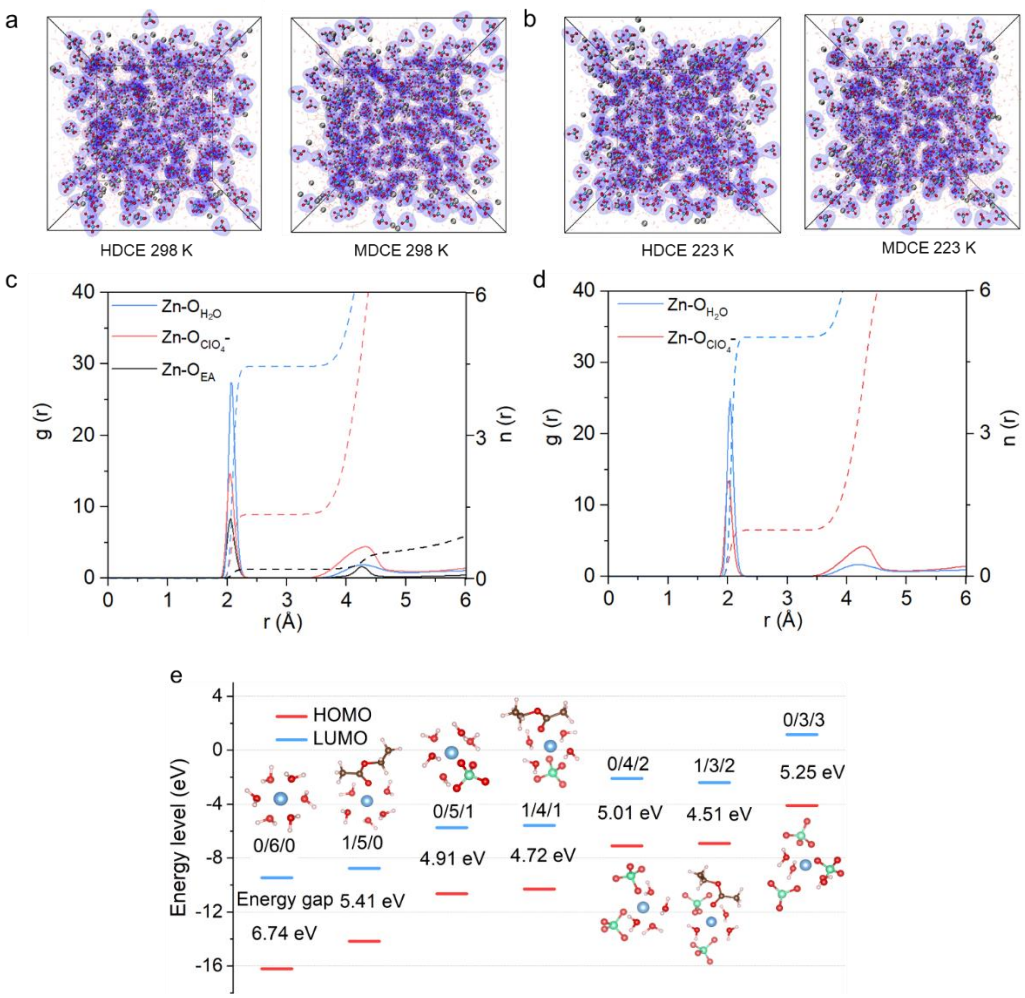

Supplementary Fig. 11 (a,b) Snapshots of representative Zn^{2+} solvation motifs in HDCE and MDCE at 25 °C (a) and -50 °C (b); anion distributions are highlighted. (c,d) Distributions of Zn^{2+} solvation species and RDFs/CNs in MDCE (c) and HDCE (d) at 25 °C. (e) HOMO/LUMO energy levels and molecular orbitals for solvation structures in HDCE and MDCE; structures are defined by the local fractions of EA/H_2O/ClO_4^-.

More details are provided for the MD simulations: The parameters of Zn^{2+} were obtained from previously reported research[7], ($R_{min,M}/2$ = 1.373Å, ε_M = 0.01179373 kcal mol^{-1}). The parameters of ClO_4^- and EA were generated with Sobtop[8]. The simulations were conducted using AMBER force field with the OPC water model. The production MD simulation was performed for 20 ns with a time step of 1 fs using the leap-frog integrator. Bond constraints were handled using the LINCS algorithm with an order of 4 and one iteration. A Verlet cutoff scheme was employed for neighbor searching with a frequency of 10 steps. Both the short-range electrostatic and van der Waals cutoffs were set to 1.0 nm. Long-range electrostatic interactions were treated using the Particle Mesh Ewald (PME) method with a fourth-order interpolation and a Fourier grid spacing

of 0.16 nm. The temperature was maintained at 298 K or 223K using the Nosé-Hoover thermostat with a time constant of 0.5 ps applied to the system. The pressure was controlled at 1.0 bar using the Parrinello-Rahman barostat with isotropic coupling, a time constant of 2.0 ps, and a compressibility of 4.5×10^{-5} bar^{-1}. Periodic boundary conditions were applied in all three directions.

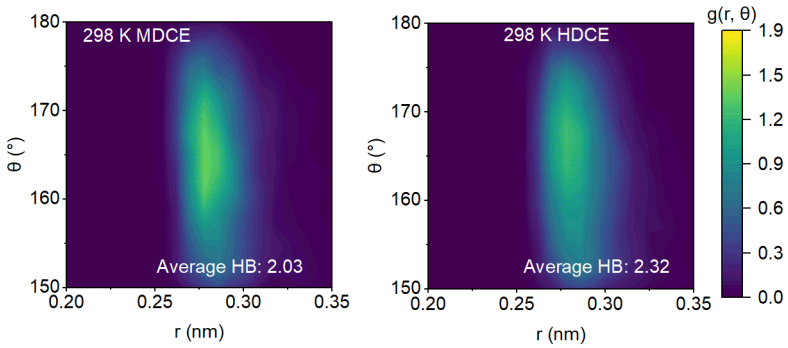

Supplementary Fig. 12 Radial angular distribution functions, g(r, θ), for MDCE and HDCE at 298 K.

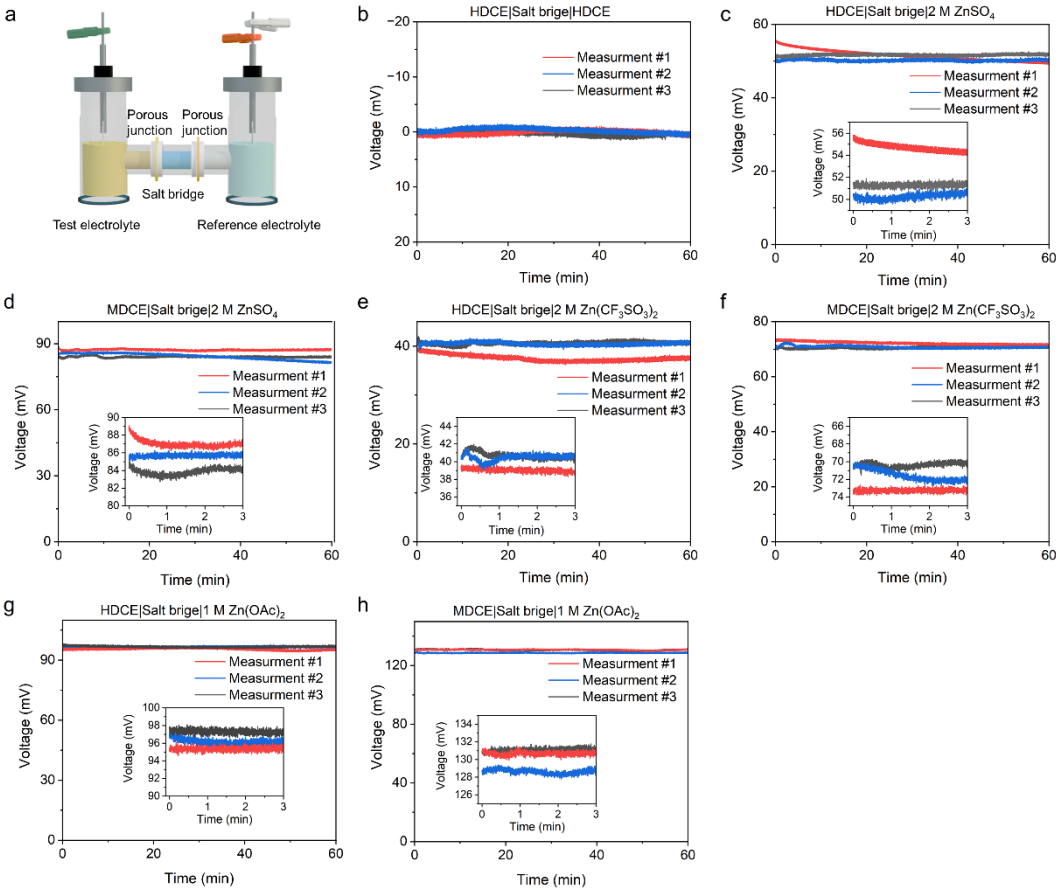

Supplementary Fig. 13 Potentiometric measurement of relative Zn^{2+} solvation energy. (a) H-cell setup: two Zn electrodes, each immersed in a different electrolyte, a reference electrolyte (EL_{ref}) and a test electrolyte (EL_{test}). The open-circuit cell voltage E_cell reports the difference in Zn^{2+} solvation free energy between EL_{test} and EL_{ref} (ΔG = -nFE _cell; see Supplementary Discussion S1). (b) Representative voltage trace for HDCE vs an aqueous reference electrolyte. (c–h) HDCE (c,e,g) and MDCE (d,f,h) measured against 2 M $ZnSO_{4(aq)}$, 2 M $Zn(CF_3SO_3)_{2(aq)}$, and 1 M $Zn(OAc)_{2(aq)}$, respectively. A typical measurement is completed within 3 min with negligible mixing-induced drift; over 60 min, drift is approximately 1–2 mV.

Supplementary Note 6

In our experiments, the open circuit potential measurement yields a positive electrical potential. A more positive open-circuit potential between two electrolytes (reference and test) indicates a more negative free energy of solvation. The Gibbs free energy of solvation ($\Delta G_{solvation}$) is converted from the measured H-cell open-circuit voltage ($E_{H\text{-}cell}$) using the formula: ΔG = -nFE. The Gibbs free energy of solvation is all a general

assessment of the strength of the binding (how much the Gibbs energy is reduced) between Zn^{2+} and the surrounding substances (solvent and anions).

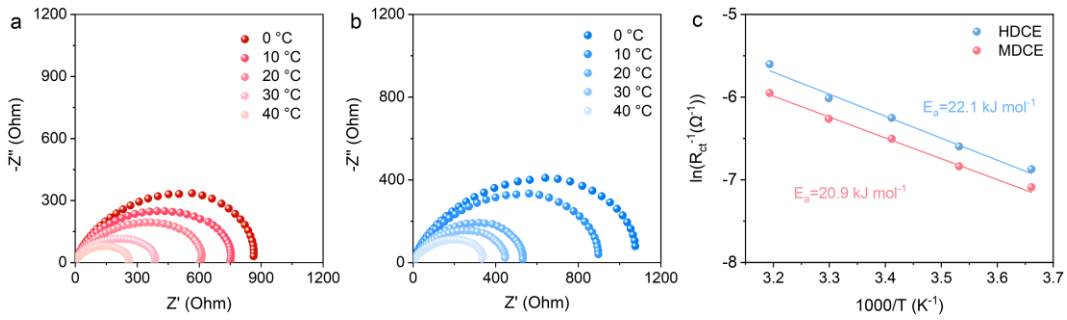

Supplementary Fig. 14. a,b, Nyquist plots of Zn||Zn cells with MDCE (a) or HDCE (b) electrolyte. c, Arrhenius plots and the activation energies of R_{ct} derived from the Nyquist plots of Zn||Zn cells with HDCE or MDCE electrolyte.

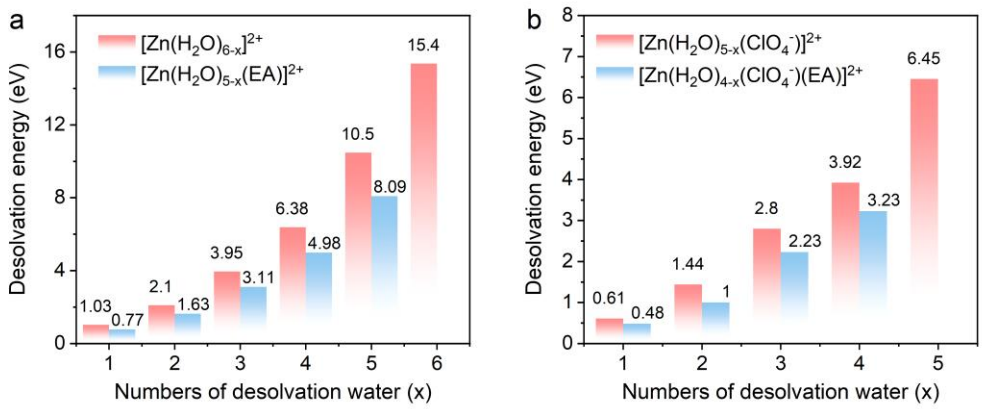

Supplementary Fig. 15 (a,b) Desolvation energy values of Zn^{2+}-solvent complex with EA and without EA obtained by DFT.

Supplementary Note 7

The calculation method for removing a water molecule is based on the difference in desolvation energy between different hydrated zinc ions. For example, we subtracted 4.89 from 8.09 to get 3.11. This indicates that the desolvation energy for $[Zn(H_2O)_{6-x}]^{2+}$ removing one water molecule to become $[Zn(H_2O)_{5-x}]^{2+}$ is 3.11 eV.

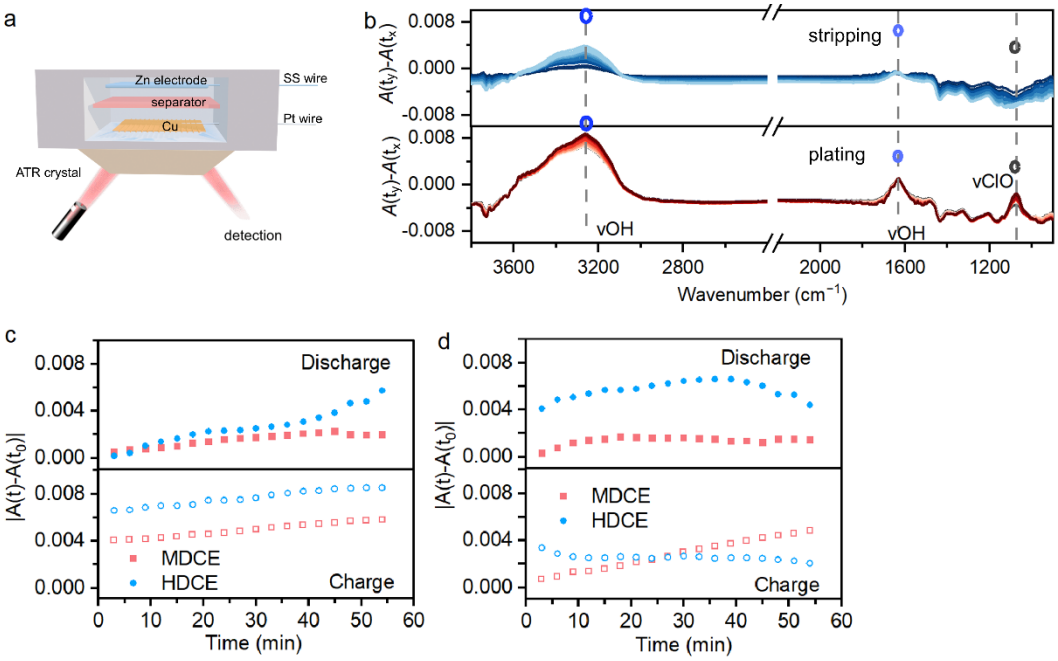

Supplementary Fig. 16 a, Schematic of spectra-electrochemical cell carried out for *in situ* FTIR measurements at the interface of Cu/electrolyte. b, The $A(t_y)$-$A(t_x)$ relative absorbance evolution during discharging (top, blue) and charging (bottom, red). which depicts the evolution of O−H stretching vibration of interfacial H_2O (νOH) and Cl−O stretching antisymmetric vibration of ClO_4^- (νClO) in HDCE. (the bule circle indicate the peaks of H_2O, the grey circle indicate the peaks of ClO_4^-). c, d, The absorption intensity $|A(t_x) - A(t_0)|$ evolution of νOH (c) and νClO (d) with increasing time of applied voltage.

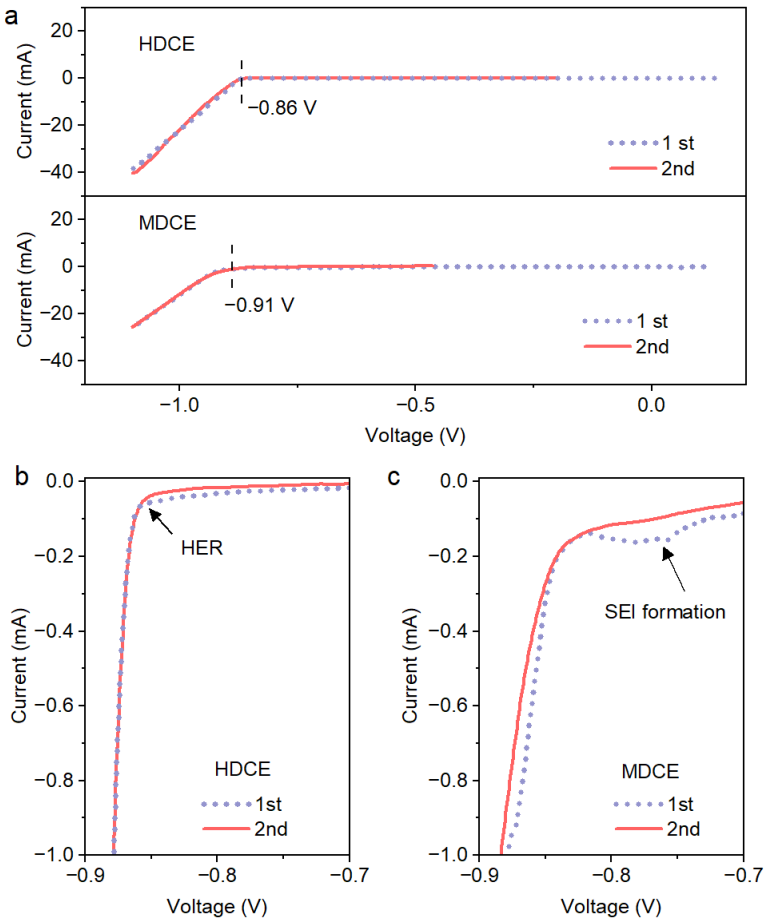

Supplementary Fig. 17 (a) Full-scale LSV and magnified views for (b) HDCE and (c) MDCE, recorded with Cu foil (working), Zn metal (counter), and Ag/AgCl (reference), Scan rate: 0.5 mV s^{-1}, from 0.2 V to −1.2 V.

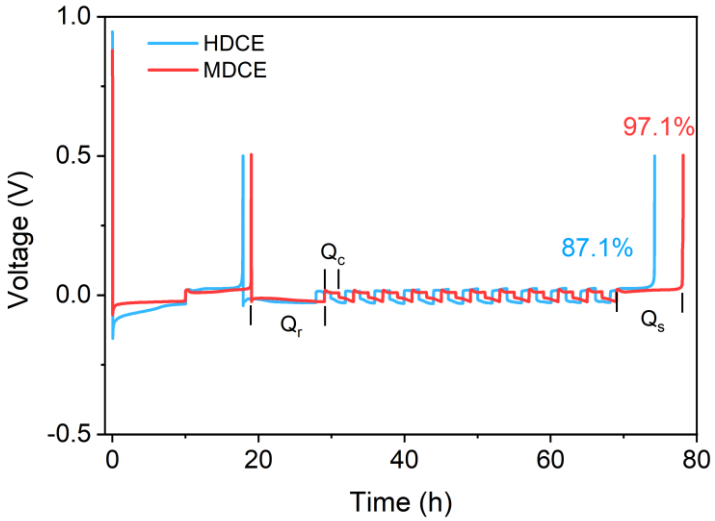

Supplementary Fig. 18 Plating/stripping profiles for CE determination in MDCE and HDCE at 0.5 mA cm^{-2}.

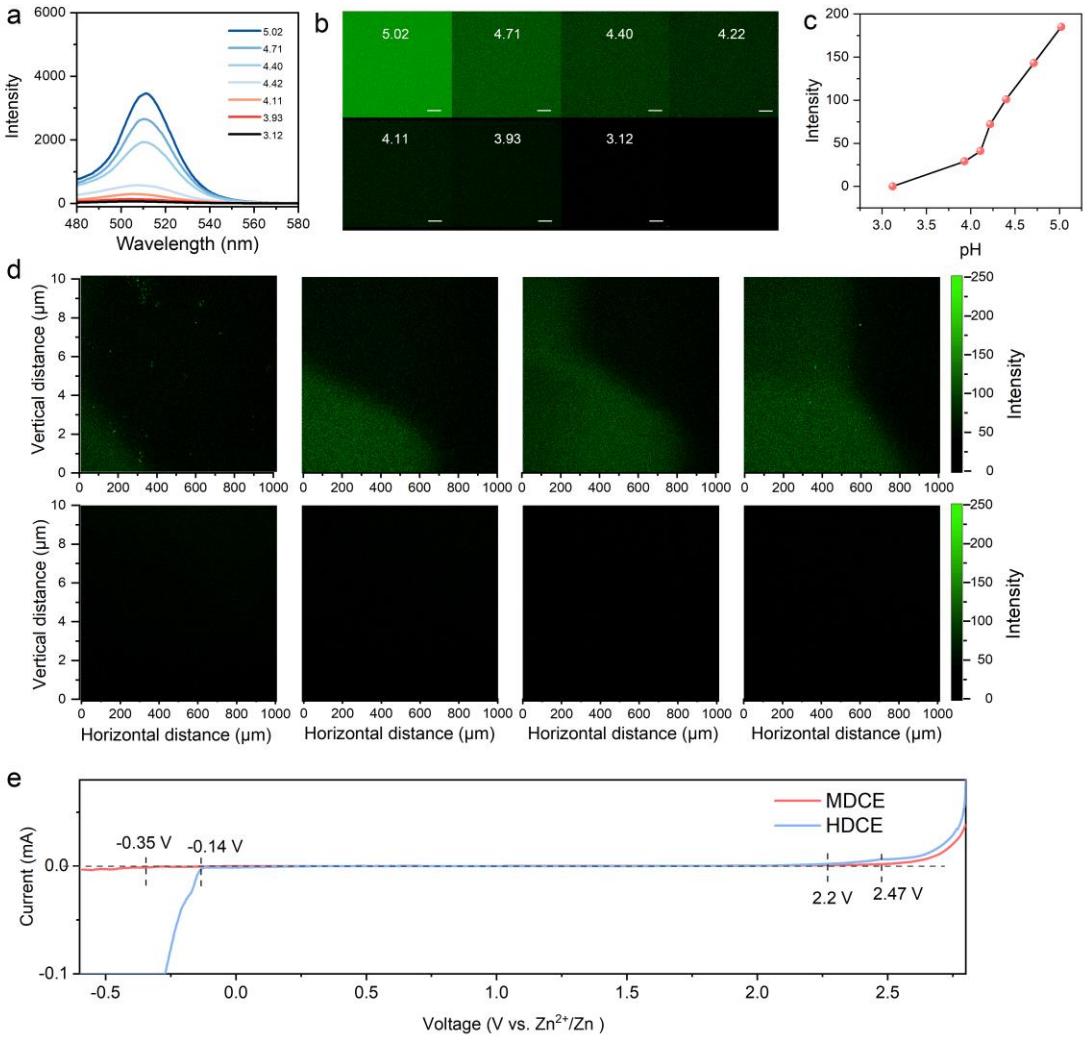

Supplementary Fig. 19 Characterization of the electrolyte containing HPTS. a, Fluorescence emission spectra of 500 μM HPTS in HDCE in the pH range of 3.12 to 5.02. b, CLSM images recorded in the HDCE electrolyte containing 500 μM HPTS with pH varying from 3.12 to 5.02. c, Calibration results for the pH dependence of the fluorescent electrolyte. An exponential function is fitted for pH below 4 and a linear function is fitted for pH above 4. d, Time sequence of the fluorescence distributions in HDCE (upper) and MDCE (below) during the process of Zn^{2+} deposition on Zn foil (assembled as a Zn||Zn cell). e, Electrochemical window of the designed Zn||SS asymmetric cell with HDCE and MDCE measured by LSV at 1 $mV \cdot s^{-1}$.

Supplementary Note 8

The fluorescence emission spectra of HDCE containing 500 μM HPTS revealed a gradual increase in fluorescence intensity from low to high pH, with a peak at approximately 510 nm (Supplementary Fig. 18a). Electrolyte samples across a range of

pH values were analyzed using confocal microscopy within the specified excitation and emission range, enabling quantification of fluorescence intensity (Supplementary Fig. 18b). A calibration curve correlating fluorescence intensity to pH was established (Supplementary Fig. 18c). This relationship was quantified by fitting an exponential function for pH values below 4 and a linear function for pH values of 4 and above. Concurrently, the HER was suppressed, with the onset potential shifting from −0.14 V to −0.35 V. LSV measurements further demonstrated that the anodic stability of MDCE improved to 2.47 V (versus Zn/Zn^{2+}), compared to 2.20 V for HDCE.

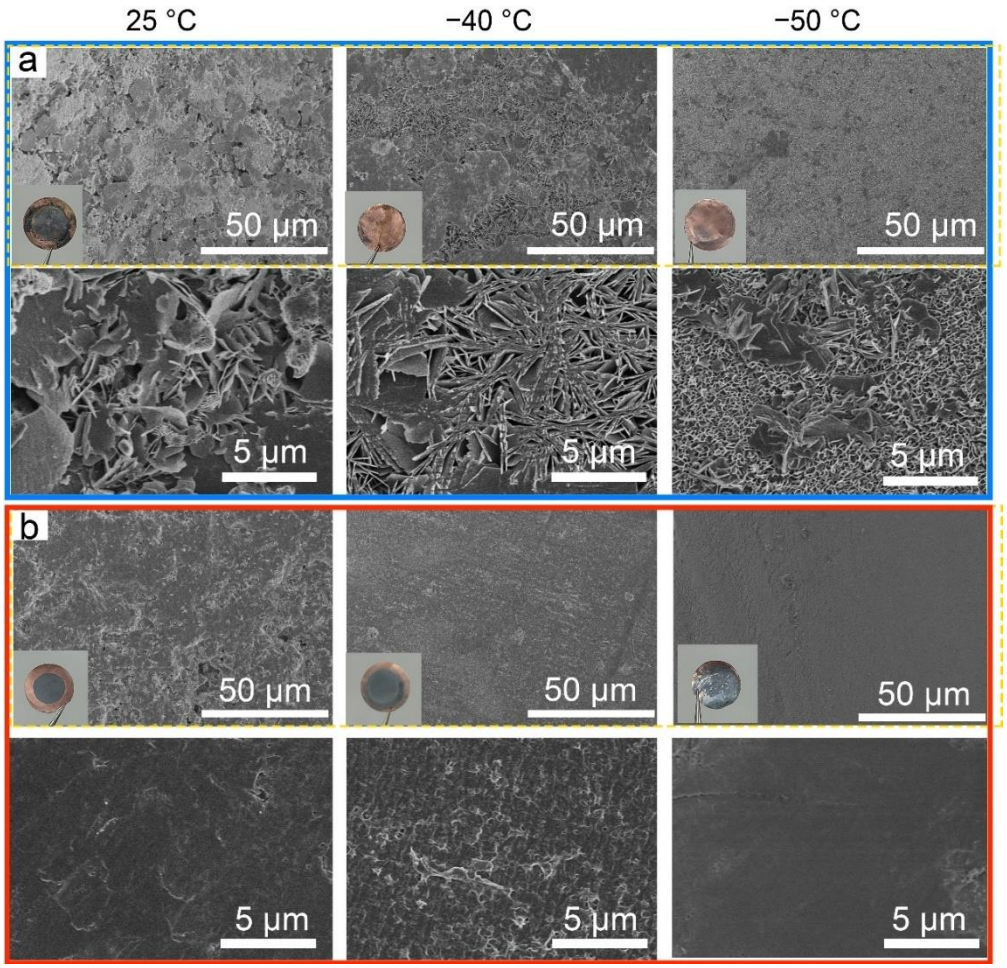

Supplementary Fig. 20 a,b, SEM images of Zn plated in HDCE (a) and MDCE (b).

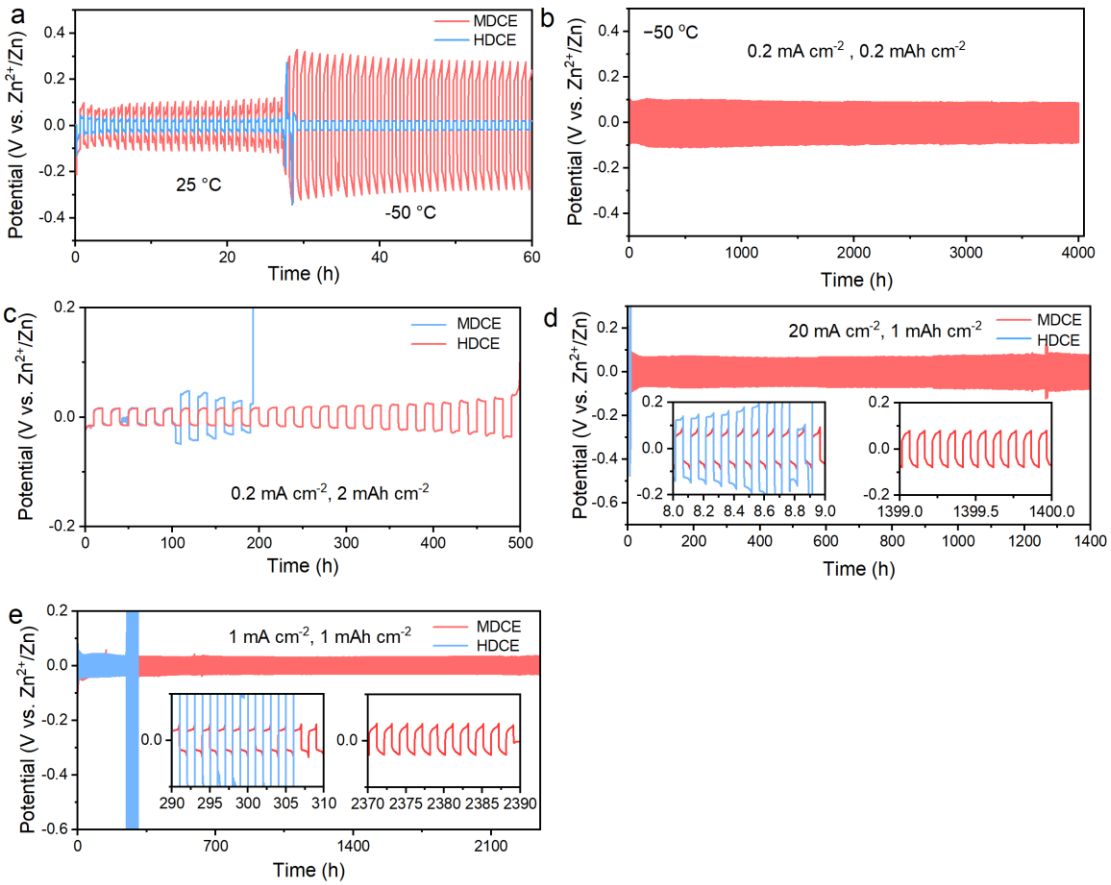

Supplementary Fig. 21 a, Plating/stripping profiles of the investigated electrolytes in symmetric Zn||Zn cells at various temperatures, the unstable voltages displayed by the HDCE system are attributed to short circuit events. b, Zn plating/stripping performance of the Zn|MDCE|Zn cells at −50 °C. c, Discharge/charge curves of symmetric Zn||Zn cells at 0.2 mA cm^{-2} and 2.0 mAh cm^{-2}, (each cycle lasts for 10 h). d,e, Discharge/charge curves of symmetric Zn||Zn cells at 20 mA cm^{-2}, 1 mAh cm^{-2} (d) and 1 mA cm^{-2}, 1 mAh cm^{-2} (e).

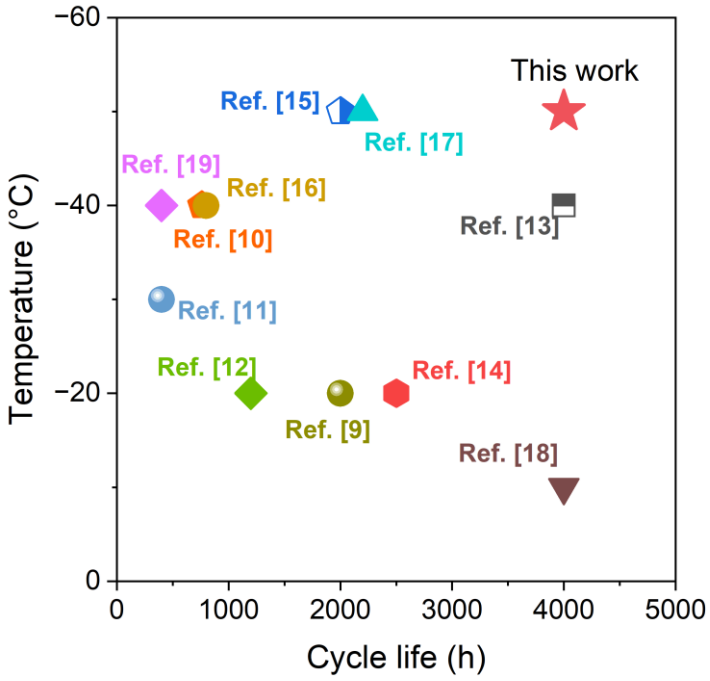

Supplementary Fig. 22 Comparison of the cycle life values of aqueous electrolyte in Zn||Zn cells at −50 °C-0 °C[9-19].

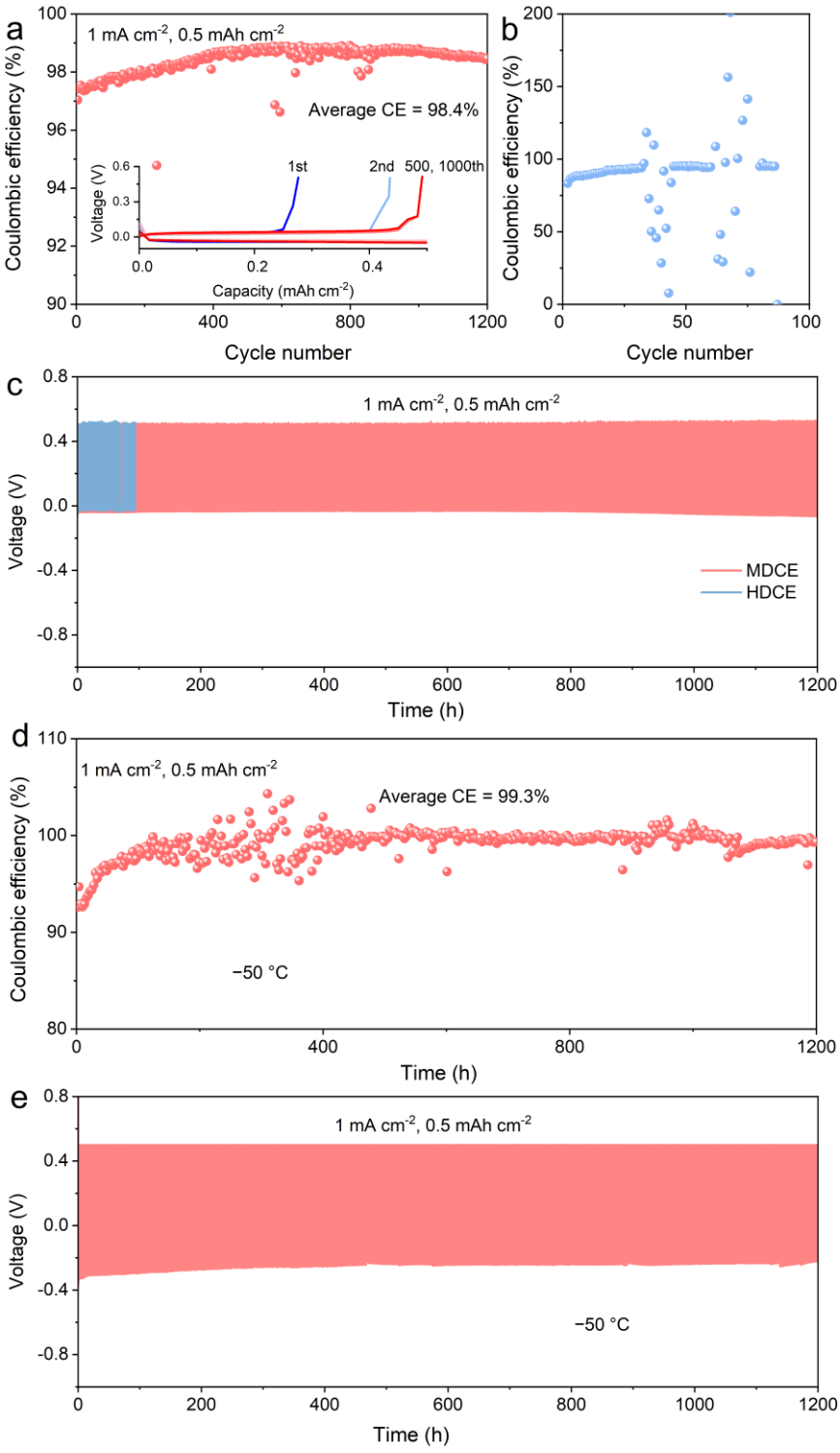

Supplementary Fig. 23 a, The typical charge-discharge curves (inset: potential vs capacity) of Zn||Cu cells cycled in MDCE, and Coulombic efficiency vs cycle number of Zn||Cu cells with the MDCE. b, Coulombic efficiency vs cycle number of Zn||Cu cells with the HDCE. c, The discharge-charge curves Zn||Cu cells cycled in HDCE and MDCE. d,e, CE vs cycle time (d) and the discharge-charge curves (e) of Zn||Cu cells cycled in MDCE at 1 mA cm $^{-2}$, 0.5 mAh cm $^{-2}$ and −50 °C.

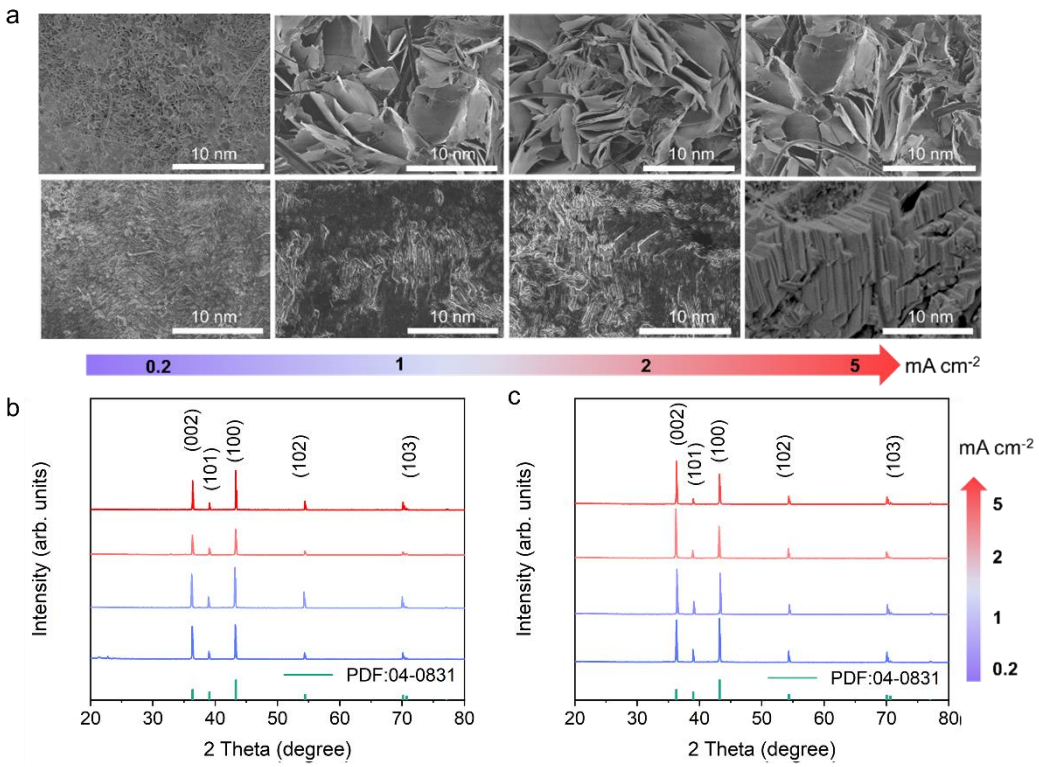

Supplementary Fig. 24 a, Morphological evolution of zinc deposited in HDCE (top) and MDCE (bottom) at different current densities. b,c, Crystallographic orientation of zinc deposited in HDCE (b) and MDCE (c) at different current densities.

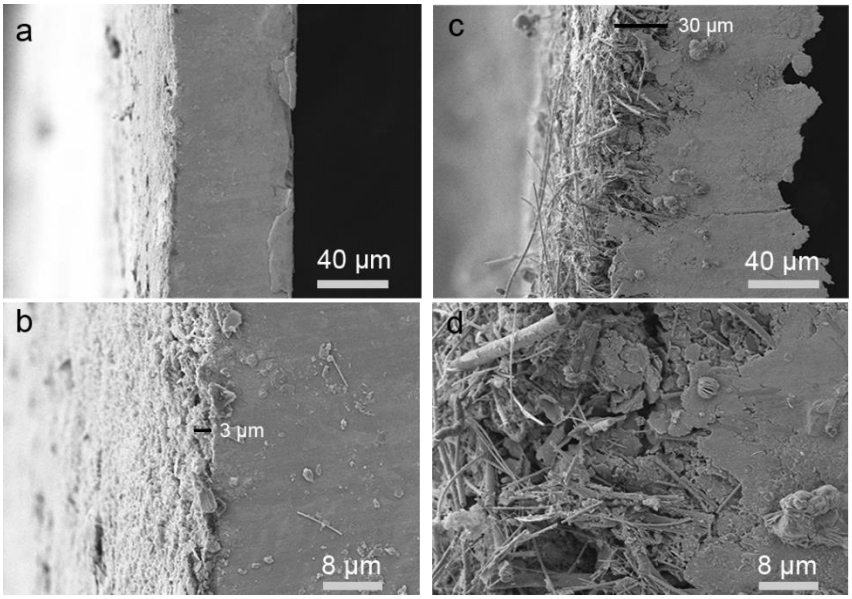

Supplementary Fig. 25 a,b,c,d, SEM images of Zn metal cross-section of Zn electrodes at plating state with MDCE (a, b) and HDCE (c, d) electrolytes at 1 mA cm^{-2} and 1 mAh cm^{-2} (50 cycles).

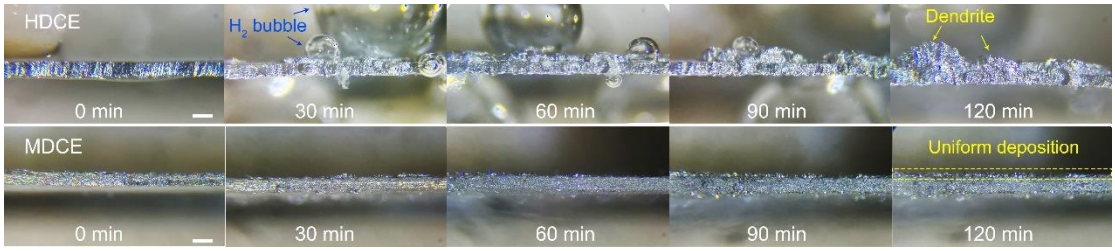

Supplementary Fig. 26 *In situ* optical microscopy images of Zn plating in HDCE and MDCE at a current density of 10 mA cm^{-2} and up to 120 min. Scale bar, 80 μm.

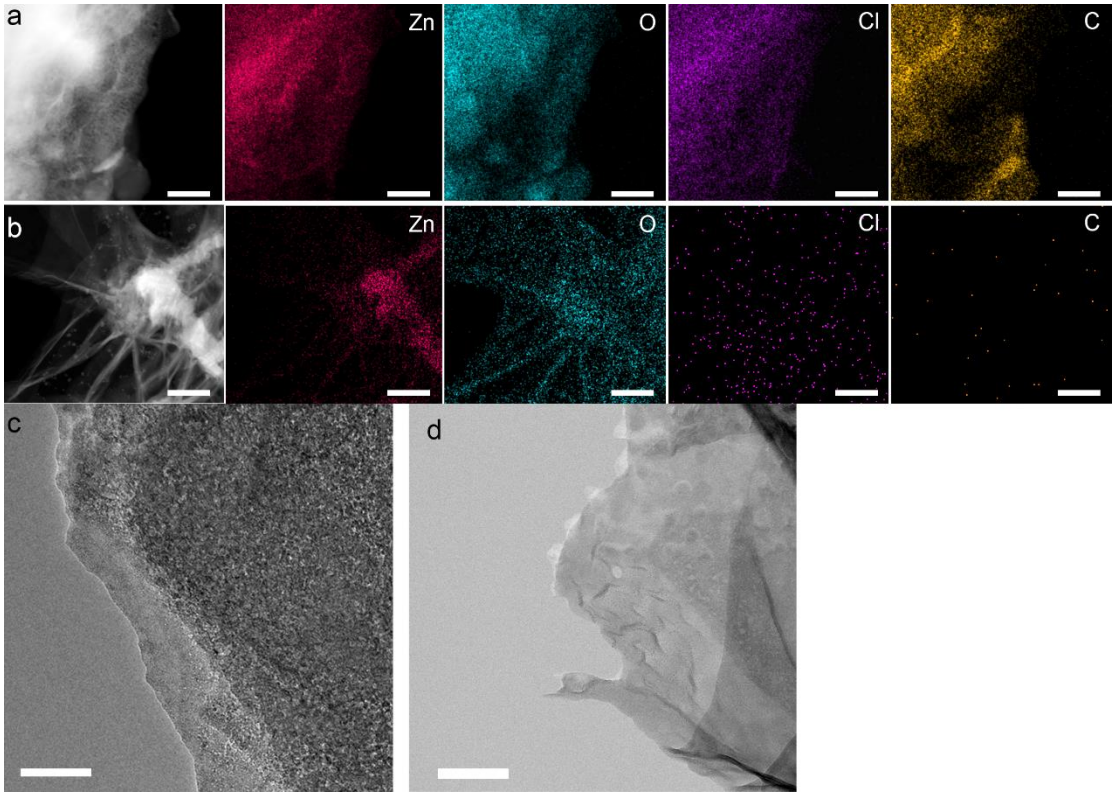

Supplementary Fig. 27. a,b, High-angle annular dark field (HAADF)/EDS analyses showing elemental mapping of Zn, O, Cl and C of Zn electrodes cycled in MDCE (a) and HDCE (b). Scale bar: 100 nm. c,d, High-resolution cryo-TEM images of Zn electrodes cycled in MDCE (c) and HDCE (d) electrolytes for 30 cycles. Scale bar: 100 nm.

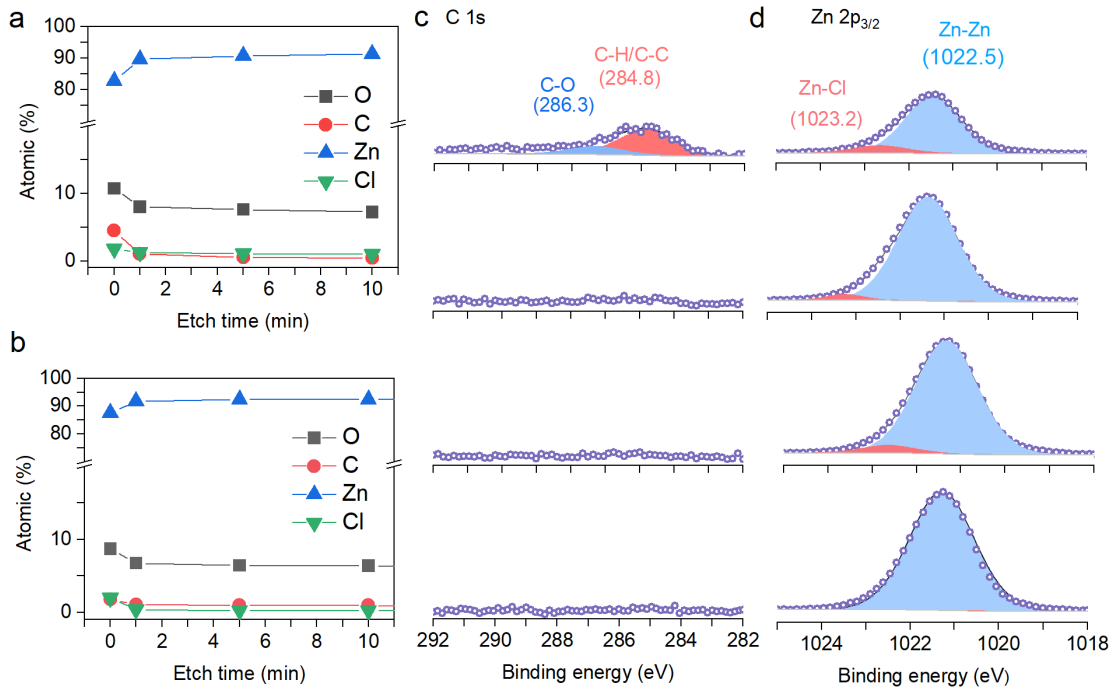

Supplementary Fig. 28 a,b, Composition of the SEI revealed by X-ray photoelectron spectroscopy (XPS) after various durations of Ar^+ sputtering on Zn surface cycled in HDCE (a) and MDCE (b). The sputtering removal rate is ~6 nm min^{-1}. c,d, XPS results with depth profiles of the C 1s (c) and Zn $2p_{3/2}$ (d) spectra of Zn cycled in HDCE electrolyte.

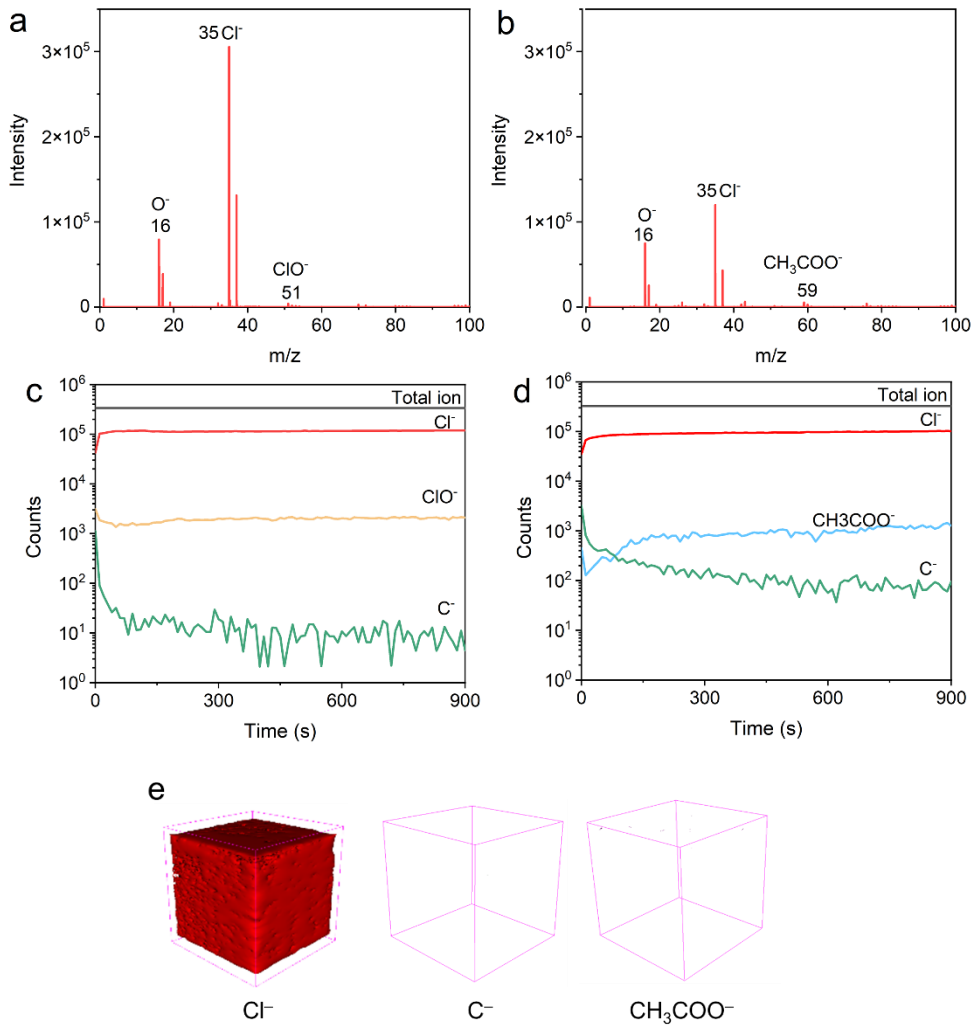

Supplementary Fig. 29 a,b, Mass spectrometry of cycled Zn anode in HDCE (a) and MDCE (b). c,d, ToF-SIMS depth profiling of several typical second ion fragments on the cycled Zn metal electrode surface in the HDCE (c) and MDCE (d), respectively. e, Three-dimensional view of Cl^-, C^- and CH_3COO^- fragments distributions of Zn anode in the TOF-SIMS sputtered volumes. The Zn anode was obtained after 30 cycles of galvanostatic plating/stripping in HDCE electrolyte (Zn||Zn cells at 1 mA cm^{-2} with a capacity of 1 mAh cm^{-2} for each half cycle).

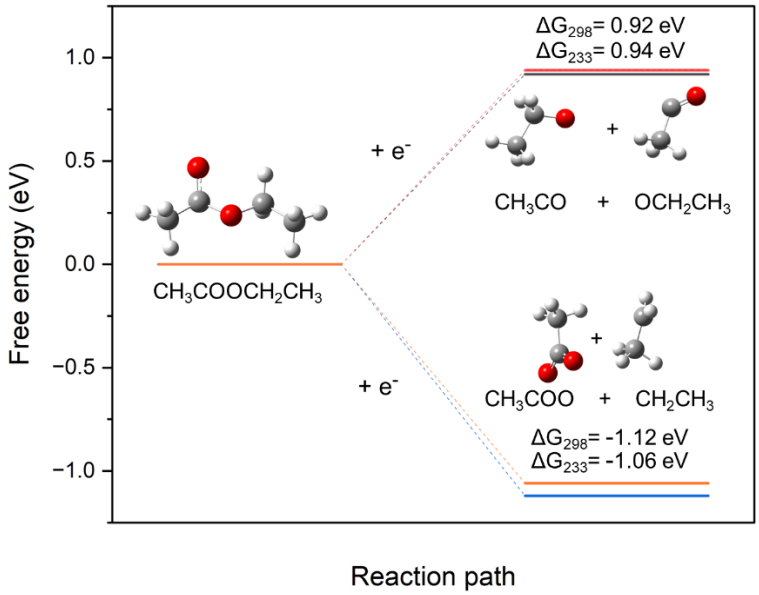

Supplementary Fig. 30 Calculated reaction energetics (Delta G) for the electron-induced reduction and decomposition of EA.

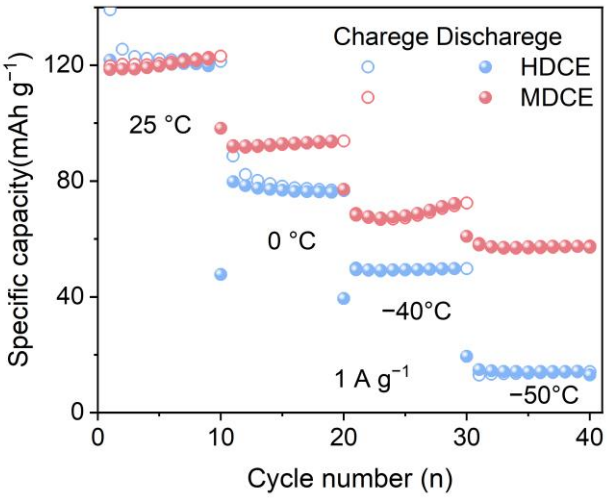

Supplementary Fig. 31 Rate capability of the PANI|HDCE|Zn and PANI|MDCE|Zn cells from 25 °C to −50 °C.

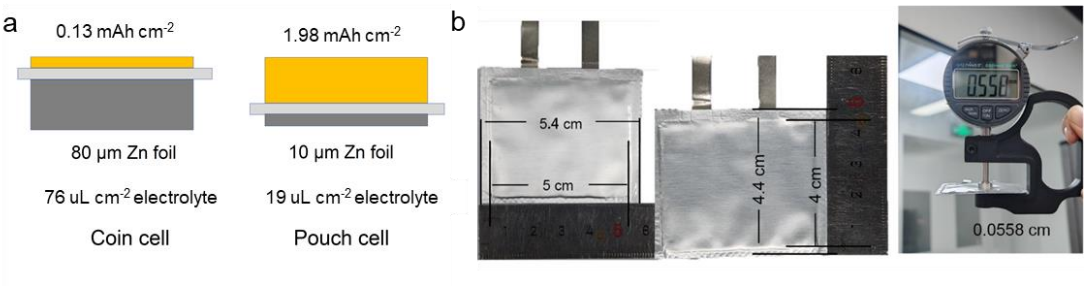

Supplementary Fig. 32 a, Comparison of pouch cell and coin cell in terms of N/P, E/C and areal capacity. b, The size of the Zn||PANI pouch cell.

Supplementary Tables

Supplementary Table 1. Comparative of solvent properties, including donor number, dielectric constant, freezing point, and viscosity.

Solvent	Donor number	Freezing point (°C)	η (mPa·s)	ε
EA	**17.2**	**−83.6**	**1.9**	**6.4**
PC	15.0	−49.2	2.5	64.9
DMSO	29.8	−19.0	2.0	48.9
EG	20.0	−12.9	25.66	37.0
DMF	26.6	−62.0	1.0	36.7
AN	14.0	−48.0	0.34	35.7
MeOH	19.0	−97.5	0.59	32.7
THF	20.0	−108.5	0.55	7.6
TMP	23.0	−46.0	1.76	21.3
DMC	17.2	4.0	0.59	3.1
EC	16.0	35.0	1.90	90.1
H_2O	**33.0**	**0**	**0.85**	**78.46**

Supplementary Table 2. The price of conventional organic solvents from Sigma Aldrich.

Salt	Price (USD mL^{-1})
EA	**0.023**
butanone[20]	0.14
ethylene glycol[21]	0.089
acetonitrile[22]	0.087
tetrahydrofuran[23]	0.83
trimethyl phosphate[24]	0.126
sulfolane[25,26]	0.05
N,N-dimethylformamide[27]	0.173
diglyme[28]	0.288

Supplementary Table 3. The price of Zn salts from Sigma Aldrich.

Salt	Price (USD g^{-1})	Concentration (M)*
$Zn(ClO_4)_2 \cdot 6H_2O$	**0.336**	**2**
$ZnSO_4$ $7H_2O$	0.89	2
$Zn(OTF)_2$	5.08	1-3
$ZnCl_2$	0.296	7-30
$Zn(TFSI)_2$	128	0.2
$Zn(BF_4)_2 \cdot xH_2O$	3.15	4
$Zn(OAc)_2 \cdot 2H_2O$	3.29	30

*Electrolyte concentrations which are frequently studied in the reported literature.

The price of Zn salts from Sigma Aldrich (2025).

Supplementary Table 4. Temperature-dependent ionic conductivity of 2 M $Zn(ClO_4)_2$ in H_2O/EA across EA:H_2O ratios from 0:1 to 1:6, measured with a conductivity meter.

Electrolytes	σ (mS cm^{-1})				
EA/H_2O molar ratios	25 °C	0 °C	-20 °C	-40 °C	-50 °C
0:1	105.01	94.78	84.28	--	--
1:20	69.37	66.5	52.22	27.37	24.5
1:16	64.47	54.11	45.71	25.69	24.92
1:12	61.11	57.26	45.36	24.29	19.88
1:8	48.37	44.52	34.23	16.45	14.49
1:6	45.71	42.56	34.09	14.7	12.88

Supplementary Table 5. Curve-fitting parameters for Zn K-edge EXAFS of $Zn(H_2O)_5(ClO_4)^+$ and $Zn(H_2O)_4EA(ClO_4)^+$ standards. Reported parameters: coordination number (C.N.), bond distance (R), Debye–Waller factor (σ^2), inner potential correction (ΔE_0), and R-factor (goodness of fit). S_0^2 was fixed at 0.85.

Sample	Path	R (Å)	C. N.	$\sigma^2\times10^3$ (Å^2)	ΔE_0 (eV)	R factor
Zn	Zn-Zn	2.64	6	12.9	−0.038	0.009
HDCE (path in $Zn(H_2O)_5(ClO_4)^+$)	Zn-O (H_2O)	2.13	5.1	6.4	−1.8	0.007
	Zn-O (ClO_4)	2.09	0.9			
MDCE(path in $Zn(H_2O)_4EA(ClO_4)^+$)	Zn-O (H_2O)	2.15	3.4	9.6	−2.6	0.013
	Zn-O (ClO_4)	2.08	1.5			
	Zn-O (EA)	2.18	1.1			

Supplementary Table 6. Solvation energies for each electrolyte.

Solvent	Reference electrolyte	Voltage (V)	Solvation Energy (eV)	Solvation Energy (kJ mol^{-1})
HDCE	HDCE	0	0	0
HDCE	2 M $ZnSO_4$ H_2O	0.0529 ± 0.00017	-0.1058 ± 0.00034	-10.1568 ± 0.0326
MDCE	2 M $ZnSO_4$ H_2O	0.0860 ± 0.00110	-0.1720 ± 0.00220	-16.5954 ± 0.2123
HDCE	2 M $Zn(CF_3SO_3)_2$ H_2O	0.0401 ± 0.00007	-0.0774 ± 0.00014	-7.7381 ± 0.0135
MDCE	2 M $Zn(CF_3SO_3)_2$ H_2O	0.0718 ± 0.00012	-0.1386 ± 0.00232	-13.8552 ± 0.0232
HDCE	1 M $Zn(OAc)_2$ H_2O	0.0960 ± 0.00017	-0.1853 ± 0.00033	-18.5251 ± 0.0328
MDCE	1 M $Zn(OAc)_2$ H_2O	0.1301 ± 0.00009	-0.2511 ± 0.00174	-25.1054 ± 0.0174

Supplementary Table 7 | Comparison of the cycle life values of aqueous electrolyte based $ZnCl_2$, $Zn(ClO_4)_2$ and other state-of-the-art strategies developed for high-efficiency anodes of Zn metal batteries.

Anode	Electrolyte	Current density (mA cm^{-2})	Areal capacity (mAh cm^{-2})	Cycle life (h)	References
Zn	$Zn(ClO_4)_2$ in H_2O/EA	**0.2**	**0.2**	**7200**	
		0.2	2	500	
		1	1	2390	
		20	**1**	**1400**	
		0.2	**0.2**	**4000 (−50 °C)**	
		1	**1**	**2840 (−50 °C)**	
Zn	$Zn(ClO_4)_2 \cdot 6H_2O$/SN ratio of 1:8	0.2	2	400	[21]
		0.05	0.5	800	
Zn	30 m $ZnCl_2$ + 5 m LiCl + 10 m TMACl	1	1	2000	[29]
		5	5	Over 800	
Zn	1 M $Zn(OTF)_2$ in H_2O/PC	1	0.5	1600	[30]
Zn	$ZnCl_2$ in EG with molar ratio 1:4	0.5	0.5	2000	[31]
	0.5M $Zn(OTF)_2$ in TMP	1	1	Over 2300	[32]
	0.5M $Zn(TFSI)_2$ + 0.05M TFMP in AN	2.5	2.5	~800	[33]
Zn	1M $Zn(PS)_2$+0.2 TBATS	1	1	2000	[34]
		3	3	1000	
Zn	$ZnSO_4$-C_3N_4QDs	1	1	1200	[35]
Zn	$Zn(Ac)_2$/Fad	0.5	0.5	1400	[36]

Supplementary references

1 Bard, A. J., Faulkner, L. R. & White, H. S. Electrochemical methods: Fundamentals and applications, -2nd Edition. (Wiley Textbooks, 2000).

2 Wang, H., Kim, S. C., Rojas, T., Zhu, Y., Li, Y., Ma, L., Xu, K., Ngo, A. T. & Cui, Y. Correlating Li-ion solvation structures and electrode potential temperature coefficients. *J. Am. Chem. Soc.* **143**, 2264-2271 (2021).

3 Kim, S. C., Kong, X., Vilá, R. A., Huang, W., Chen, Y., Boyle, D. T., Yu, Z., Wang, H., Bao, Z., Qin, J. & Cui, Y. Potentiometric measurement to probe solvation energy and its correlation to lithium battery cyclability. *J. Am. Chem. Soc.* **143**, 10301-10308 (2021).

4 Chen, X. & Zhang, Q. Atomic insights into the fundamental interactions in lithium battery electrolytes. *Acc. Chem. Res* **53**, 1992-2002 (2020).

5 Hou, R., Guo, S. & Zhou, H. Atomic insights into advances and issues in low-temperature electrolytes. *Adv. Energy Mater.* **13**, 2300053 (2023).

6 Uematsu, M. & Franck, E. U. Static dielectric constant of water and steam. *J. Phys. Chem. Ref. Data* **9**, 1291-1306 (1980).

7 Li, Z., Song, L. F., Li, P. & Merz, K. M., Jr. Systematic parametrization of divalent metal ions for the OPC3, OPC, TIP3P-FB, and TIP4P-FB water models. *J. Chem. Theory Comput.* **16**, 4429-4442 (2020).

8 Lu, T. Sobtop, version 1.0(dev5), http://sobereva.com/soft/Sobtop (2025).

9 Xiong, P., Kang, Y., Yao, N., Chen, X., Mao, H., Jang, W.-S., Halat, D. M., Fu, Z.-H., Jung, M.-H., Jeong, H. Y., Kim, Y.-M., Reimer, J. A., Zhang, Q. & Park, H. S. Zn-ion transporting, in situ formed robust solid electrolyte interphase for stable zinc metalanodes over a wide temperature range. *ACS Energy Lett.* **8**, 1613-1625 (2023).

10 Zhang, L., Han, Y., Geng, Y., Zhang, H., Liu, H., He, Y., Yan, Z. & Zhu, Z. Aqueous zinc-ion batteries with boosted stability and kinetics under a wide temperature range. *Angew. Chem., Int. Ed.* **64**, e202500434 (2025).

11 Zhang, Q., Xia, K., Ma, Y., Lu, Y., Li, L., Liang, J., Chou, S. & Chen, J. Chaotropic anion and fast-kinetics cathode enabling low-temperature aqueous zn batteries. *ACS Energy Lett.* **6**, 2704-2712 (2021).

12 You, C., Wu, R., Yuan, X., Liu, L., Ye, J., Fu, L., Han, P. & Wu, Y. An inexpensive electrolyte with double-site hydrogen bonding and a regulated Zn^{2+} solvation structure for aqueous Zn-ion batteries capable of high-rate and ultra-long low-temperature operation. *Energy Environ. Sci.* **16**, 5096-5107 (2023).

13 Ma, Q., Gao, R., Liu, Y., Dou, H., Zheng, Y., Or, T., Yang, L., Li, Q., Cu, Q., Feng, R., Zhang, Z., Nie, Y., Ren, B., Luo, D., Wang, X., Yu, A. & Chen, Z. Regulation of outer solvation shell toward superior low-temperature aqueous zinc-ion batteries. *Adv. Mater.* **34**, 2207344 (2022).

14 Yu, F.-D., Yi, Z.-J., Li, R.-Y., Lin, W.-H., Chen, J., Chen, X.-Y., Xie, Y.-M., Wu, J.-H., Lan, Z., Que, L.-F., Liu, B.-S., Luo, H. & Wang, Z.-B. Temperature inversion enables superior stability for low-temperature Zn-ion batteries. *J. Energy Chem.* **91**, 245-253 (2024).

15 Wan, J., Wang, R., Liu, Z., Zhang, S., Hao, J., Mao, J., Li, H., Chao, D., Zhang, L. & Zhang, C. Hydrated eutectic electrolyte induced bilayer interphase for high-performance aqueous Zn-ion batteries with 100 °c wide-temperature range. *Adv. Mater.* **36**, 2310623 (2024).

16 Bu, F., Gao, Y., Zhao, W., Cao, Q., Deng, Y., Chen, J., Pu, J., Yang, J., Wang, Y., Yang, N., Meng, T., Liu, X. & Guan, C. Bio-inspired trace hydroxyl-rich electrolyte additives for high-rate and stable Zn-ion batteries at low temperatures. *Angew. Chem., Int. Ed.* **63**, e202318496 (2024).

17 Xie, D., Liu, H.-H., Liu, C., Diao, W.-Y., Tao, F.-Y., Jiang, W.-B., Sun, H.-Z., Wang, J.-W., Yu, H., Li, W.-L., Wu, X.-L. & Zhang, J.-P. Co-solvent and additive joint engineering enable long-life and wide-temperature Zn metal battery. *Energy Stor. Mater.* **70**, 103524 (2024).

18 You, S., Deng, Q., Wang, Z., Chu, Y., Xu, Y., Lu, J. & Yang, C. Achieving highly stable Zn metal anodes at low temperature via regulating electrolyte solvation structure. *Adv. Mater.* **36**, 2402245 (2024).

19 Zha, Z., Li, D., Sun, T., Sun, Q., Hou, J., Tao, Z. & Chen, J. Electrolyte design via cation–anion association regulation for high-rate and dendrite-free zinc metal batteries at low temperature. *J. Am. Chem. Soc.* **146**, 31612-31623 (2024).

20 Shi, X., Xie, J., Wang, J., Xie, S., Yang, Z. & Lu, X. A weakly solvating electrolyte towards

practical rechargeable aqueous zinc-ion batteries. *Nat. Commun.* **15**, 302 (2024).
21 Han, D., Cui, C., Zhang, K., Wang, Z., Gao, J., Guo, Y., Zhang, Z., Wu, S., Yin, L., Weng, Z., Kang, F. & Yang, Q.-H. A non-flammable hydrous organic electrolyte for sustainable zinc batteries. *Nature Sustainability* **5**, 205-213 (2021).
22 Yang, W., Du, X., Zhao, J., Chen, Z., Li, J., Xie, J., Zhang, Y., Cui, Z., Kong, Q., Zhao, Z., Wang, C., Zhang, Q. & Cui, G. Hydrated eutectic electrolytes with ligand-oriented solvation shells for long-cycling zinc-organic batteries. *Joule* **4**, 1557-1574 (2020).
23 Wang, D., Peng, H., Zhang, S., Liu, H., Wang, N. & Yang, J. Localized anion‐cation aggregated aqueous electrolytes with accelerated kinetics for low‐temperature zinc metal batteries. *Angew. Chem., Int. Ed.* **62** (2023).
24 Wang, W., Chen, S., Liao, X., Huang, R., Wang, F., Chen, J., Wang, Y., Wang, F. & Wang, H. Regulating interfacial reaction through electrolyte chemistry enables gradient interphase for low-temperature zinc metal batteries. *Nat. Commun.* **14**, 5443 (2023).
25 Li, C., Kingsbury, R., Thind, A. S., Shyamsunder, A., Fister, T. T., Klie, R. F., Persson, K. A. & Nazar, L. F. Enabling selective zinc-ion intercalation by a eutectic electrolyte for practical anodeless zinc batteries. *Nat. Commun.* **14**, 3067 (2023).
26 Wang, Y., Wang, T., Bu, S., Zhu, J., Wang, Y., Zhang, R., Hong, H., Zhang, W., Fan, J. & Zhi, C. Sulfolane-containing aqueous electrolyte solutions for producing efficient ampere-hour-level zinc metal battery pouch cells. *Nat. Commun.* **14**, 1828 (2023).
27 Qiu, X., Wang, N., Wang, Z., Wang, F. & Wang, Y. Towards high‐performance zinc‐based hybrid supercapacitors via macropores‐based charge storage in organic electrolytes. *Angew. Chem., Int. Ed.* **60**, 9610-9617 (2021).
28 Kang, Y. C., Zhang, F., Li, H. Z., Wei, W. R., Dong, H. T., Chen, H., Sang, Y. H., Liu, H. & Wang, S. H. Modulating the electrolyte inner solvation structure via low polarity co-solvent for low-temperature aqueous zinc-ion batteries. *Energy Environ. Mater.*, e12707 (2024).
29 Jiang, H., Tang, L., Fu, Y., Wang, S., Sandstrom, S. K., Scida, A. M., Li, G., Hoang, D., Hong, J. J., Chiu, N.-C., Stylianou, K. C., Stickle, W. F., Wang, D., Li, J., Greaney, P. A., Fang, C. & Ji, X. Chloride electrolyte enabled practical zinc metal battery with a near-unity Coulombic efficiency. *Nat. Sustain.* **6**, 806-815 (2023).
30 Ming, F., Zhu, Y., Huang, G., Emwas, A.-H., Liang, H., Cui, Y. & Alshareef, H. N. Co-solvent electrolyte engineering for stable anode-free zinc metal batteries. *Am. Chem. Soc.* **144**, 7160-7170 (2022).
31 Geng, L., Meng, J., Wang, X., Han, C., Han, K., Xiao, Z., Huang, M., Xu, P., Zhang, L., Zhou, L. & Mai, L. Eutectic electrolyte with unique solvation structure for high-performance zinc-ion batteries. *Angew. Chem., Int. Ed.* **61**, e202206717 (2022).
32 Naveed, A., Yang, H., Shao, Y., Yang, J., Yanna, N., Liu, J., Shi, S., Zhang, L., Ye, A., He, B. & Wang, J. A highly reversible zn anode with intrinsically safe organic electrolyte for long-cycle-life batteries. *Advanced Materials* **31**, 1900668 (2019).
33 Ma, L., Pollard, T. P., Schroeder, M. A., Luo, C., Zhang, Y., Pastel, G., Cao, L., Zhang, J., Shipitsyn, V., Yao, Y., Wang, C., Borodin, O. & Xu, K. Engineering a zinc anode interphasial chemistry for acidic, alkaline and non-aqueous electrolytes. *Energy Environ. Sci.* **17**, 2468-2479 (2024).
34 Chen, S., Ji, D., Chen, Q., Ma, J., Hou, S. & Zhang, J. Coordination modulation of hydrated zinc ions to enhance redox reversibility of zinc batteries. *Nat. Commun.* **14**, 3526 (2023).
35 Zhang, W., Dong, M., Jiang, K., Yang, D., Tan, X., Zhai, S., Feng, R., Chen, N., King, G., Zhang, H., Zeng, H., Li, H., Antonietti, M. & Li, Z. Self-repairing interphase reconstructed in each cycle for highly reversible aqueous zinc batteries. *Nature Communications* **13**, 5348 (2022).
36 Li, J., Lou, Y., Zhou, S., Chen, Y., Zhao, X., Azizi, A., Lin, S., Fu, L., Han, C., Su, Z. & Pan, A. Intrinsically decoupled coordination chemistries enable quasi-eutectic electrolytes with fast kinetics toward enhanced zinc-ion capacitors. *Angew. Chem. Int. Ed.* **63**, e202406906 (2024).